




Article

Wildfire Smoke Particle Properties and Evolution, from Space-Based Multi-Angle Imaging

Katherine Junghenn Noyes ^{1,*}, Ralph Kahn ², Arthur Sedlacek ³, Lawrence Kleinman ³, James Limbacher ^{2,4,5} and Zhanqing Li ^{1,6}

- ¹ Department of Atmospheric and Oceanic Science, University of Maryland, College Park, MD 20742, USA; zhanqing@umd.edu
- ² Earth Science Division, NASA Goddard Space Flight Center, Greenbelt, MD 20771, USA; ralph.a.kahn@nasa.gov (R.K.); james.limbacher@nasa.gov (J.L.)
- ³ Environmental and Climate Sciences Department, Brookhaven National Laboratory, Upton, NY 11973, USA; sedlacek@bnl.gov (A.S.); kleinman@bnl.gov (L.K.)
- ⁴ Science Systems and Applications Inc., Lanham, MD 20706, USA
- ⁵ Department of Meteorology and Atmospheric Science, the Pennsylvania State University, State College, PA 168026, USA
- ⁶ Earth System Science Interdisciplinary Center, College Park, MD 20740, USA
- * Correspondence: junghenn@umd.edu

Received: 30 January 2020; Accepted: 26 February 2020; Published: 29 February 2020



Abstract: Emitted smoke composition is determined by properties of the biomass burning source and ambient ecosystem. However, conditions that mediate the partitioning of black carbon (BC) and brown carbon (BrC) formation, as well as the spatial and temporal factors that drive particle evolution, are not understood adequately for many climate and air-quality related modeling applications. In situ observations provide considerable detail about aerosol microphysical and chemical properties, although sampling is extremely limited. Satellites offer the frequent global coverage that would allow for statistical characterization of emitted and evolved smoke, but generally lack microphysical detail. However, once properly validated, data from the National Aeronautics and Space Administration (NASA) Earth Observing System's Multi-Angle Imaging Spectroradiometer (MISR) instrument can create at least a partial picture of smoke particle properties and plume evolution. We use in situ data from the Department of Energy's Biomass Burning Observation Project (BBOP) field campaign to assess the strengths and limitations of smoke particle retrieval results from the MISR Research Aerosol (RA) retrieval algorithm. We then use MISR to characterize wildfire smoke particle properties and to identify the relevant aging factors in several cases, to the extent possible. The RA successfully maps qualitative changes in effective particle size, light absorption, and its spectral dependence, when compared to in situ observations. By observing the entire plume uniformly, the satellite data can be interpreted in terms of smoke plume evolution, including size-selective deposition, new-particle formation, and locations within the plume where BC or BrC dominates.

Keywords: biomass burning; remote sensing; MISR; smoke plumes; aerosol particle properties; aerosols; BBOP; multi-angle; multi-spectral; wildfire

1. Introduction

Wildfires are significant emitters of trace gases and aerosols that impact local air quality, and they can affect regional- and global-scale radiation budgets, cloud properties, and the water cycle. As such, adequately representing wildfire smoke plumes is an important consideration in climate and air quality modeling. In addition to dust storms, wildfires are the most significant sources of light-absorbing aerosols globally, specifically involving brown carbon (BrC) and black carbon (BC),

as well as purely scattering aerosols, all of which have wide-ranging environmental impacts. Smoke aerosols that escape the planetary boundary layer (PBL) have the potential to stay aloft for several days or more, altering the regional radiative budget on time scales that can extend beyond the age of the fire itself and can affect air quality hundreds of kilometers downwind [1,2]. These particles also have the potential to act as cloud-condensation nuclei (CCN), resulting in aerosol–cloud interactions that can alter cloud reflectivity, cloud lifetime, and the frequency of precipitation [3–6].

The fuel type and amount, fire regime, and meteorology are known to affect smoke plume aerosol composition, with evidence indicating systematic differences in particle size distribution, particle light absorption, and the spectral dependence of absorption (e.g., References [7–10]). Although the dominant absorbing aerosol in biomass burning smoke is often BC, which is highly absorbing across all visible wavelengths, there is a variable fraction of BrC as well, which is usually less absorbing overall and exhibits stronger absorption at shorter wavelengths. For example, studies suggest higher BrC fractions in smoke plumes from smoldering than from flaming fires [11–13]. However, we do not yet have much understanding, even qualitatively, relating fire type to smoke particle speciation, nor of the fire-type-specific properties of BrC, which vary greatly (e.g., Reference [14]). Furthermore, the mixing state of biomass burning (BB) aerosol particles is dynamic, changing with time and distance from the source, as they interact with water vapor, trace gases, and other particles during aging. For example, aerosols can oxidize in the presence of water vapor and other gaseous compounds, increasing the single scattering albedo (SSA) and possibly altering hygroscopicity so that they become more effective CCN. Larger particles might experience preferential gravitational settling, leading to an aerosol size distribution that is both narrower and, on average, smaller. Coatings deposited on particles increase their size, which, in turn, can increase scattering efficiency and enhance SSA as the plume ages [14,15]. Coatings deposited on BC particles can sometimes enhance light absorption through a lensing effect. As a plume cools, increased ambient relative humidity can result in increased particle hydration, SSA, and mean diameter. Gas-to-particle conversion can also occur where volatile organic compounds (VOCs) or SO₂ emissions are present, which can produce very small and bright aerosols that might subsequently coagulate with primary aerosols. These mechanisms can occur in combinations that change on relatively short temporal and spatial scales. The variable nature of BB particles means that smoke plume radiative and other environmental impacts are far from uniform or predictable at present, especially as the dominant factors mediating particle aging are uncertain.

Significant efforts were made in recent years to observe smoke particle properties in situ with laboratory experiments, stationary observation sites (e.g., Reference [16]), and aircraft field campaigns. Recent field campaigns in the United States (US) include the Department of Energy's Biomass Burning Observation Project (BBOP) [17,18] and the National Aeronautics and Space Administration (NASA)'s Studies of Emissions and Atmospheric Composition, Clouds, and Climate Coupling by Regional Surveys (SEAC⁴RS) [19]. These experiments studied both wildfire gas and particle-phase plume chemistry in great detail; in many cases, they were able to detect and measure different aerosol compositions within wildfire plumes (e.g., References [20–22]). The in situ observations provide data for only a small set of BB smoke cases, and in themselves do not allow for statistical characterization of emitted and evolved smoke. They do, however, provide considerable detail about aerosol microphysical properties, such as SSA and size distribution, which, in the past, were comparatively less well represented in satellite retrievals and models.

Due to the observational limitations mentioned above, much is unknown about the temporal and spatial distribution of fire-generated particle types and their aging. To date, most climate models do not discriminate between BC and BrC even though these particles display distinctly different physical, chemical, and optical properties (e.g., References [14,23]). Models are also uncertain about the role wildfire smoke plays in the aerosol–cloud interaction. Better characterization of BB aerosol properties is important to climate modeling, as it can improve our ability to quantify the radiative impacts of wildfires, which are expected to increase in frequency and intensity with global warming.

Such increases would result in increased BB aerosol loading in the free troposphere, potentially causing more intense and longer-lasting environmental effects.

Until recently, satellite remote sensing data were relatively unhelpful in painting a sufficiently detailed, large-scale picture of aerosol properties. Early work focused primarily on retrieving the optical depth of ultraviolet (UV)-absorbing species, with considerable uncertainties due to sensitivity of the results to the vertical distribution of the smoke and the contributions of other aerosol types [24,25]. With the help of newly developed techniques, we are now in a position to improve our characterization of BB particles globally, and to explore the factors that control emitted and evolved BB particle properties (e.g., Reference [26]). In the current paper, we demonstrate several such techniques that leverage the multi-angle, multi-spectral measurements from the Multi-Angle Imaging Spectrometer (MISR) instrument aboard the NASA Earth Observing System's Terra satellite. The methods rely on retrievals from the MISR Interactive Explorer (MINX) tool to calculate plume heights and associated wind vectors [27], and the MISR Research Aerosol (RA) retrieval algorithm to characterize particle properties [28,29]. Recently, changes in particle size and light absorption observed with the RA were associated with particle coalescence, hydration, oxidation, gravitational sorting, and other processes in volcanic plumes [30–34]. Here, we both demonstrate the strengths and limitations of the MISR RA in retrieving wildfire smoke plume particle properties and explore the degree to which the results can go further than in situ observations in providing information on the entirety of the plume and its immediate surroundings. As the signal/noise for particle property retrievals is highest when the aerosol optical depth (AOD) is substantial [35], aerosol plumes are especially good targets for such analysis.

The goal of the current paper is to explore the degree to which these MISR methods can qualitatively describe plume particle characteristics, setting the stage for future work at developing a global climatology of BB aerosol plume properties and processes. A partial validation of the RA is conducted here with the aim of placing on firmer ground MISR retrievals of smoke plumes that are less well constrained by field observations. This is done primarily with data obtained during the BBOP campaign, on the 21 August 2013 flight through the Government Flats Complex Fire in northern Oregon, for which there was a near-coincident MISR overpass (~2 h difference). Additional case studies presented here, having larger time differences between aircraft and satellite observations, bolster the comparison efforts and illustrate how the RA can help create a timeline of plume particle evolution, especially when combined with other coincident and noncoincident observations.

Data sources and analysis methods are outlined in Section 2. Section 3 presents our analyses of the similarities and differences between the RA and aircraft observations for the Government Flats Complex Fire, and briefly summarizes results for two additional BBOP campaign fires for which the aircraft and MISR observations were ~24 h apart. The aerosol property differences determined from remote sensing illustrate how unique data signatures can point to certain aerosol aging processes and plume evolution mechanisms. Finally, conclusions and plans for future work are given in Section 4.

2. Materials and Methods

Any comparison between satellite data and in situ observations is inherently challenging. The main obstacles are as follows: (1) satellite measurements probe large atmospheric volumes at comparatively low spatial resolution (~1 km), whereas in situ observations are collected at higher spatial resolution (~10–100 m), but cover only a fraction of the area seen from space, often lacking context and making large-scale averaging and interpretation difficult; (2) satellite observations of the atmosphere are affected by the presence of clouds, sun elevation effects, surface reflectance contributions, instrument degradation, and errors/assumptions made in the retrieval algorithms; (3) in situ instruments are subject to their own measurement uncertainties, such as sample inlet cut-off issues, typically requiring pre- or post-flight calibration; these measurements usually rely heavily on human operation, which reduces standardization; (4) passive remote sensing provides indirect measurements of column-integrated quantities that are not vertically resolved in most cases, whereas in situ suborbital data provide direct

measurements, typically at specific points in three-dimensional (3D) space, making direct comparisons with satellite observations impossible for many variables.

For the current study, we face the additional challenge of time differences on the order of hours to a day between the satellite and in situ observations. The sampling differences and limitations of each dataset determine how the comparisons have to proceed. For example, the BBOP instruments may be capable of finding extreme values, even if they sample only a small portion of the plume, whereas MISR averages the signal over ~1.1 km or more horizontally, and vertically over the column. Likewise, MISR is capable of seeing more area and may find different signals in parts of the plume that were missed by the aircraft. We address these issues by (1) focusing the comparison between the satellite and aircraft data on the general *trends* in aerosol properties along the length of the plumes, rather than focusing on the absolute values of those properties at particular locations, and (2) considering the possibility that differences in spatial and temporal sampling between the data might contribute to some observed differences in reported aerosol properties. Because smoke plume particle properties often evolve rapidly only a short time after they are emitted, where possible, we compare locations sampled by the aircraft and satellite of similar estimated plume age.

2.1. Case Selection and Fire Properties

Fire properties (i.e., burning characteristics, fuel type, etc.) can change dramatically over short time periods, making it difficult to compare in situ observations with satellite observations if there is a significant time difference. Thus, only flights that were coincident or near-coincident with the MISR observations can be used for the primary validation study. Among the BBOP flights, only one was near-coincident with MISR: the 21 August 2013 flight through a smoke plume in northern Oregon dubbed the Government Flats Complex Fire; the flight began approximately 2 h after MISR observed the area (Figure 1, Table 1). During the time between observations, plume geometry changed noticeably, most likely as a result of wind-driven advection. However, as shown later, plume particle properties still correlate reasonably well, especially for plume elements of similar age.

Table 1. Flight dates, times, and locations compared with dates and times of the Multi-Angle Imaging Spectroradiometer (MISR) overpass of the same area. Positive time delays between satellite and aircraft observations indicate the satellite observed the fire after the aircraft, whereas negative numbers mean the satellite completed its overpass first. The last flight, on 21 August, is the focus of the validation portion of the study. UTC—Universal Coordinated Time.

Fire Identifier	Aircraft Observations			MISR Observations			
	Date (UTC)	Start Time–End Time (UTC) ^a	Location	Date (UTC)	Orbit; Block (s)	Time (UTC)	Approximate Delay (h)
Colockum Tarps	26/7/13	20:00–22:20	Southern central WA	7/27/13	72382; 53–54	19:13	+23
Douglas Complex	06/8/13	19:30–21:00	Southern coastal OR	8/5/13	72513; 56	19:08	–23
Government Flats	21/8/13	21:20–22:30	Northern central OR	8/21/13	72746; 54	19:07	–2

^a Indicates the approximate time range that the aircraft was actively observing the smoke plume(s) rather than the total flight time.

The second phase of this study uses the same type of data from other BBOP flights that took place approximately one day apart from MISR overpasses, the Colockum Tarps Fire and the Douglas Complex Fire (Table 1). Although these cases are less useful for validating the RA, they serve here as examples of the versatile and fluid nature of BB aerosol microphysical and optical properties. They also demonstrate the potential of the RA as a tool that both complements and enhances knowledge gained from in situ observations of wildfire smoke plumes.

2.2. MISR

The unique multi-angle imaging capability of the MISR instrument [36] enables height and motion vector retrievals for clouds and aerosol plumes. Plume height is retrieved geometrically, based on the parallax of contrast features within the plume as observed in the multi-angle views. As such, plume features must have sufficient optical thickness and contrast, relative to the surface, to obtain plume height with this method. The retrievals are nicely accomplished by the MISR Interactive Explorer (MINX) software tool [27,37], which was used to derive stereo heights and wind vectors for plumes in this study. With MINX, heights and winds are retrieved locally by first manually defining the plume source, plume extent, and wind direction from the MISR imagery. MINX was used in a variety of studies, including but not limited to retrieving heights and winds for volcano, wildfire, and dust plumes [27,30,32–34,38–43]. Retrieved plume height and wind vectors help constrain aerosol transport modeling used to determine smoke source and age, and they can indicate whether the plume was injected above the PBL. The MINX analysis also provides some initial insight into the quality of the viewing conditions, as plumes lacking a clear source or easily identifiable wind direction in the satellite imagery can result in low-confidence height retrievals. In addition, if the plume height is above about 2 km, the MISR images must be co-registered at the median plume height rather than at ground level to maximize aerosol-type retrieval performance when subsequently using the RA.

The MISR RA [28,29] was used to constrain aerosol optical depth (AOD), as well as particle extinction Ångström exponent (ANG), single scattering albedo (SSA), and shape, all indicative of “aerosol type.” A wide variety of aerosol components, each having different microphysical properties, can be included in the RA climatology, depending on the intended use of the algorithm (e.g., volcanic plumes, dust plumes, pollution, or wildfire plumes). The particle property information content of MISR observations is qualitative, amounting to three to five size bins (e.g., “small,” “medium,” and “large”), two to four bins in SSA, and spherical vs. randomly oriented non-spherical particle shapes, under good but not necessarily ideal retrieval conditions [35,44].

In this work, we refer to the retrieved information on particle size and light absorption as the *retrieved effective particle size* (REPS; μm) and the *retrieved effective particle absorption* (REPA; dimensionless), respectively. Particle size and light absorption derived from the satellite data are based on column-integrated, optical measurements rather than from direct sampling; thus, these terms help reflect both the measured content and the limitations of the retrieved quantities. Particle property information is diminished when the mid-visible AOD is below about 0.15 or 0.2, but this is not an issue for well-defined smoke plumes. For the current study, we included one non-spherical component (a soil or dust grain optical analogue, based on an optical model derived by Lee et al. [45]) and 16 spherical components covering a range of sizes and SSA values (Table 2). For absorbing aerosols, the RA further classifies particle type according to flat or steep spectral dependence, where “flat” aerosols display little to no spectral variation in absorption and represent urban pollution or BC particles, whereas “steep” aerosols have greater absorption at shorter wavelengths and are more akin to BrC from wildfire smoke [8,14,28,46]. For each MISR pixel, the RA calculates component AOD values such that the simulated top-of-atmosphere (TOA) reflectances best match the MISR multi-angle, multi-spectral observations. This method was used for global aerosol typing [35] and for characterizing particle type in volcanic plumes [30,33,34]. Furthermore, along-plume changes in AOD, REPS, and REPA combined with available meteorological data and MINX stereo heights can provide insight into the relevant aging mechanisms for a plume observed under good retrieval conditions. For example, constant or increasing AOD accompanied by decreasing REPS can indicate the formation of secondary aerosols. Conversely, constant AOD accompanied by increasing REPS may indicate particle aggregation. Decreasing AOD accompanied by decreasing REPS may indicate size-selective dilution. These and other patterns were observed with MISR in volcanic plumes [34].

The operation of the RA was described by Limbacher and Kahn [28,29]. Recently, several advancements were made to the RA that increase particle property sensitivity, especially for over-land retrievals, and are leveraged in the current study. Most importantly, the RA uses

prescribed land-surface reflectances from the Moderate Resolution Imaging Spectroradiometer (MODIS) Multi-Angle Implementation of Atmospheric Correction (MAIAC) [47]. In some previous RA versions, the surface reflectances were retrieved by the RA itself, which made it more difficult to separate the surface from atmospheric contributions, especially for optically thick, elevated plumes [44]. Secondly, the TOA reflectances are also now co-registered at the plume height, allowing results to be keyed to various heights rather than assuming confinement to the near-surface boundary layer. Thirdly, in evaluating the retrieval cost function, the algorithm now weights each channel (band and camera) based on the AOD retrieved when each aerosol mixture is assumed. The weights are normalized such that the mean value is one. This allows for effective use of the MISR near-infrared (NIR) band, which improves retrieval sensitivity to large particles. Specifically, when the surface reflectance is high in the NIR, which is often the case over land, the aerosol retrieval in that channel is likely to be poor. However, the AOD required to match the observed reflectances will also be low due to the bright surface; thus, these channels are weighted less. Lastly, the number of iterations used to identify the best-fitting AOD was increased. For this work, we introduced a revised particle climatology in the RA that is more focused on biomass burning plumes than in previous versions, such as the one used by Flower and Kahn [32–34,41]. It offers a greater range of candidate spherical particle size and absorption combinations, and it is based on size and absorption ranges identified in a recent literature review of BB particle properties [14] and informed by particle properties retrieved in situ during recent aircraft field campaigns similar to BBOP; details of the 17-component optical and physical properties included are given in Table 2.

Table 2. MISR components from Research Aerosol (RA) retrieval results, using the algorithm version summarized in Section 2.2, with a 774-mixture climatology. SSA—single scattering albedo.

Particle Size, Shape, Absorption	r_e (μm) ^a	SSA (446)	SSA (558)	SSA (672)	SSA (866)	Code ^b
Very small, spherical, strongly absorbing (flat)	0.06	0.84	0.79	0.73	0.62	VSmSphSab(f)
Very small, spherical, strongly absorbing (steep)	0.06	0.76	0.80	0.83	0.76	VSmSphSab(s)
Very small, spherical, moderately absorbing (flat)	0.06	0.92	0.89	0.86	0.78	VSmSphMab(f)
Very small, spherical, moderately absorbing (steep)	0.06	0.88	0.90	0.90	0.87	VSmSphMab(s)
Small, spherical, strongly absorbing (flat)	0.12	0.81	0.79	0.78	0.74	SmSphSab(f)
Small, spherical, strongly absorbing (steep)	0.12	0.72	0.80	0.87	0.84	SmSphSab(s)
Small, spherical, moderately absorbing (flat)	0.12	0.90	0.89	0.88	0.85	SmSphMab(f)
Small, spherical, moderately absorbing (steep)	0.12	0.85	0.90	0.93	0.92	SmSphMab(s)
Medium, spherical, strongly absorbing (flat)	0.26	0.78	0.80	0.80	0.81	MeSphSab(f)
Medium, spherical, strongly absorbing (steep)	0.26	0.70	0.80	0.88	0.89	MeSphSab(s)
Medium, spherical, moderately absorbing (flat)	0.26	0.89	0.90	0.90	0.90	MeSphMab(f)
Medium, spherical, moderately absorbing (steep)	0.26	0.83	0.90	0.94	0.94	MeSphMab(s)
Very small, spherical, non-absorbing	0.06	1.0	1.0	1.0	1.0	VSmSphNab
Small, spherical, non-absorbing	0.12	1.0	1.0	1.0	1.0	SmSphNab
Medium, spherical, non-absorbing	0.26	1.0	1.0	1.0	1.0	MeSphNab
Large, spherical, weakly absorbing	1.28	1.0	1.0	1.0	1.0	LaSphNab
Large, non-spherical, weakly absorbing	1.21	0.91	0.95	0.97	0.98	LaNspHwab

^a Each component has a designated effective radius (r_e). ^b The code for each component includes four elements: size—very small (VSm), small (Sm), medium (Me), and large (La); shape—spherical (Sph) or non-spherical (Nsp); light absorption—non-absorbing (Nab), weakly absorbing (Wab), moderately absorbing (Mab), and strongly absorbing (Sab); spectral light absorption profile—equal in all spectral bands (flat), or varying between spectral bands (steep).

2.3. Aircraft Data

The BBOP campaign was conducted to enhance understanding of the atmospheric and environmental impacts of fire-generated particles, with particular focus on atmospheric chemistry [17,18]. From July to September 2013, the Department of Energy Gulfstream-1 (G-1) research aircraft flew through wildfire plumes in the Pacific Northwest, before moving to the lower Mississippi River Valley for the month of October to study agricultural burns. This field campaign was selected for the current study because it uniquely targeted the time evolution of smoke particles during the first few hours of atmospheric aging [18]. Given the large suite of instruments with which the G-1 aircraft was equipped, we leverage instrument data focused mostly on the aerosol size distribution and optical properties to which MISR is sensitive, but meteorological and atmospheric gas chemistry measurements are considered as well. For most measurements, the high temporal resolution (1–10 s, depending on the instrument) and varying amounts of instrument noise must be taken into account when making comparisons with the MISR RA results. We, therefore, smoothed the higher-frequency aircraft data (for the G-1 aircraft at cruising speed, 1 s translates to about 100 m) by aggregating the sampled points into approximately 1.1-km clusters, taking the median value of the measurements in each cluster, and assigning it to the median time, latitude, and longitude of the cluster. This facilitates both qualitative and quantitative analysis, as the RA operates at the 1.1-km spatial resolution of MISR pixels.

2.3.1. Aerosol Optical Properties

We calculate SSA from the aerosol absorption and scattering coefficient measurements taken at 1-s intervals using the particle soot absorption photometer (PSAP) and nephelometer, respectively [48]. The nephelometer measures both total and hemispheric aerosol scattering at 450, 550, and 700 nm by detecting the aerosol-scattered light and subtracting that scattered by the air, CO₂, and SF₆ carrier gases. The nephelometer data provided were corrected using methods described by Anderson and Ogren [49], where details about the estimated instrument measurement uncertainty can also be found. The PSAP measures absorption continuously at three visible wavelengths by monitoring changes in transmittance through a filter, using a three-wavelength emitting light-emitting diode (LED) (461.6, 522.7, and 648.3 nm). As filter-based instruments tend to overestimate aerosol absorption when scattering aerosols are also present, correction methods using scattering measurements from the nephelometer, based on those described by Bond et al. [50] and Ogren [51], were applied by the field scientists. The uncertainty of the PSAP measurements is ill-defined [52]. At some points in cleaner atmospheres where the nephelometer signal approached its detection limit, small negative scattering and absorption coefficients were reported. In these cases, any scattering coefficients < −3 Mm^{−1} and absorption coefficients < −5 Mm^{−1} were ignored.

To help identify BrC, which is more absorbing in the UV than the mid-visible range and can lead to enhanced absorption when acting as a BC coating, we analyzed aerosol absorption measurements at 355 nm made by the photoacoustic soot spectrometer (PAS) [53], which made its maiden deployment during the BBOP campaign, and a photothermal interferometer (PTI) [54], operating at 532 nm. Both the PAS and the PTI measure aerosol light absorption directly, by detecting air density fluctuations that occur when the air is heated due to laser light absorbed by the aerosols. The hallmark of these techniques is their immunity to aerosol light scattering; this is incredibly useful, as scattering is usually the dominant aerosol light-extinction mechanism. Relative to traditional filter-based instruments used to measure light absorption (e.g., the PSAP), these instruments exhibit a lower signal/noise ratio, but this problem is minimal for high smoke concentrations and was further reduced with the help of passive noise suppression methods (e.g., mufflers), which were employed after the first few flights. The aerosol light scattering and absorption measurements in the instrument have an uncertainty of ±15%. In previous studies, the uncertainty of the PTI technique was measured to be 10% (95% confidence interval) when using NO₂ as a calibration standard [54].

2.3.2. Aerosol Microphysical Properties

The Cloud and Aerosol Spectrometer (CAS) and Passive Cavity Aerosol Spectrometer (PCASP) calculate aerosol concentration within discrete size bins at 1-s intervals by measuring the intensity of light scattered by aerosols. In order to more directly compare size distributions from the flight data with that of the MISR RA retrievals, we summed the concentrations of multiple, smaller size bins into larger size categories for each instrument dataset, such that the median effective radius (r_e) of each bin matches those defined by the RA aerosol climatology (Tables 2 and 3). Ranges do not match perfectly, as the RA is able to consider particle sizes at both extremes, whereas the aircraft instruments were limited to aerosols between 0.09 and 3.5 μm in diameter. Where applicable, we used the median of the concentrations provided by the CAS and PCASP datasets (Table 3). Note that the comparisons made here are based on the qualitative size bins retrieved from MISR (Section 2.2); thus, our analysis is not affected by small differences in the size bin definitions.

The hygroscopicity of organic aerosols is a useful, qualitative indicator of BC mixing state and age, as hydrophobic BC aerosols normally tend to become more hydrophilic as oxidative processes produce sticky, coagulative coatings on the aerosol, often resulting in CCN activation [55]. To determine which aerosols could act as CCN, we used measurements at 1-s intervals from the Dual Column Cloud Condensation Nuclei Counter 200 (CCN-200), which uses a vertically oriented temperature gradient within a ceramic cylinder to create a supersaturated environment where water vapor can condense onto particles. The particles that grow to at least 0.75 μm are considered activated and are then sized by the optical particle counter. The CCN-200 has two columns, one of which was kept at a supersaturation of 0.15% and the other at 0.25%. Both were maintained at approximately 600 mbar pressure throughout all the flights. The uncertainty for the instrument is less than 30% [56,57]. When discussing CCN here, we refer to CCN that activate at 0.15% supersaturation as CCN_{15} and those that activate at 0.25% supersaturation as CCN_{25} , although we focus on CCN_{15} to avoid redundancy.

Table 3. Size categories used to analyze the in situ observations. PCASP—Passive Cavity Aerosol Spectrometer; CAS—Cloud and Aerosol Spectrometer.

Size Category	Size Range (R_e , μm)	Comparable RA Components	Instruments Used ^a
Very small	0.045–0.09	VSmSphSab(f), VSmSphSab(s), VSmSphMab(f), VSmSphMab(s), VSmSphNab	PCASP
Small	0.09–0.15	SmSphSab(f), SmSphSab(s), SmSphMab(f), SmSphMab(s), SmSphNab	PCASP
Medium	0.15–0.46	MeSphSab(f), MeSphMab(f), MeSphSab(s), MeSphMab(s), MeSphNab	PCASP
Large	0.46–1.725	LaSphNab, LaNsphWab	PCASP, CAS

^a PCASP data from the July flight in this study were used with caution as they were collected with the calibration curve for water (1.33) instead of aerosol (1.58), and then converted in post-processing.

2.3.3. Air and Particle Chemistry

To account for plume dilution in our analysis, we applied ~1-s carbon monoxide (CO) measurements from a Los Gatos Integrated Cavity Output Spectroscopy (ICOS) Analyzer with $\pm 5\%$ uncertainty. CO and other trace gases are often used to account for dilution via a derived quantity known as the normalized excess mixing ratio (NEMR). The NEMR, defined as the ratio of the excess concentration of a species (compared to the background air) and the background-corrected value of CO, was used to identify secondary formation of organic aerosols (OA) and inorganic aerosols in plumes using measurements of fine particle matter ($\text{PM}_{2.5}$) and OA mass [58].

To trace plume oxidation, we used nitrogen oxide measurements from a three-channel Oxides of Nitrogen Analyzer with $\pm 10\%$ uncertainty. The extent of atmospheric processing was quantified using

an independent proxy measurement for oxidation, defined here as $-\log_{10}[\text{NO}_x/\text{NO}_y]$ [59]. NO_x , which is the steady-state mixture of NO and NO_2 , undergoes oxidation reactions to form HNO_3 , peroxyacetyl nitrate (PAN), and organic nitrates. The sum of NO_x and these oxidation products is denoted NO_y , which is nearly conserved on timescales of less than one day. Although not quantitative, the NO_x/NO_y clock was shown to correlate well with O/C ratios that are commonly used to measure photochemical oxidation and secondary organic aerosol (SOA) formation [60].

We used refractory black carbon (rBC) mass and size measurements from the single-particle soot photometer (SP2) to help characterize particle type and mixing state. The SP2 derives mass concentrations of rBC by measuring the amplitude of incandescence signals produced as rBC-containing particles traverse a continuous-wave laser beam [61,62] with a ~25% level of uncertainty. At the same time, the instrument measures the size distribution ($dN/d\log D_p$) of the rBC-containing particles ranging from aerosols as small as 0.08 μm to as large as 0.65 μm in diameter. We approximate the size of rBC-containing particles at a given point using the size bin at which the $dN/d\log D_p$ curve peaks, put here in terms of effective radius and denoted as $r_{e(\text{BC})}$. It is important to remember that the particles are distributed around this value and, thus, actual sizes include particles that fall within an approximate range of $\pm 0.005 \mu\text{m}$. It should also be noted that, unlike most other data, we did not smooth the SP2 data into ~1.1-km pixels, as its 10-s temporal resolution (~1.0–1.3-km spatial resolution) is already comparable to the spatial resolution of the MISR data. For the remainder of this paper, we refer to rBC using the more qualitative label “BC”, as this is how we describe refractory black carbon particles when using satellite data.

3. Results

The Government Flats Complex was a large system of three lightning-sparked fires: the Government Flats fire, the Blackburn fire, and the Wells Road fire. They burned near Mt. Hood in Wasco County, Oregon from 16 August to 26 August 2013. Cumulatively, these fires burned over 11,350 acres of land, although the Blackburn fire was responsible for 98% of this area. According to the US Forest Service, the fuel model in this area was summer hardwood litter [63]. The plume produced by this fire complex was observed by MISR on 21 August 2013, at ~19:07 Universal Coordinated Time (UTC), ~2 h before the BBOP G-1 aircraft began sampling the same area; the aircraft continued sampling this plume for an additional hour. At both observation times, the plume displays unique aerosol optical and physical property patterns that vary with downwind distance. We divide the MISR-observed plume into four regions based on these patterns: a near-source region (designated region I), a near-downwind region (II), a mid-downwind region (III), and a far-downwind region (IV) (Figure 1a). We calculate the approximate age of the smoke at regional boundaries using the ratio of the along-plume distance and mean wind vectors in the area derived from MINX (see Supplementary Materials, Figure S1). Based on plume age calculated by Kleinman and Sedlacek [18], and similar trends in particle properties, the BBOP-observed plume was divided into regions of similar age (Figure 1b), although the aircraft did not sample the part of the plume corresponding to region IV in the MISR imagery. In this section, we compare the particle properties retrieved from space with those obtained in situ from the aircraft measurements, paying particular attention to the *differences* between these regions. We then apply this information to current knowledge on how different aging processes affect particle properties in order to infer the active mechanisms at hand.

Only observations taken within the plume boundaries seen in Figure 1 are included in our analysis, except when comparing measurements to background values. For the MISR dataset, the boundary is a user-drawn plume outline created during the MINX retrieval. Some areas of optically very thin smoke can be seen in the imagery outside the boundary, but MISR had difficulty performing retrievals beyond a certain distance downwind (where the plume becomes thin), as can be seen by the lack of MINX plume results, and as indicated by some empty pixels in the RA retrievals shown subsequently. For the BBOP dataset, the RGB MODIS-Aqua image, acquired about 2 h after the MISR overpass, was used to draw the plume outline (Figure 1b). However, significant cloud contamination made it

challenging to determine exact boundaries in the two most downwind regions; thus, carbon monoxide and total aerosol count measurements from the aircraft were used to refine the shape (Figure 1c,d, respectively). This is also important, as plume geometry can change during the course of the flight itself; thus, the MODIS snapshot might not perfectly represent the plume as sampled by the aircraft, even without cloud contamination. Where applicable, all figures display the plume boundary as a dotted-line polygon and the dividing lines between regions as thin solid gray lines.

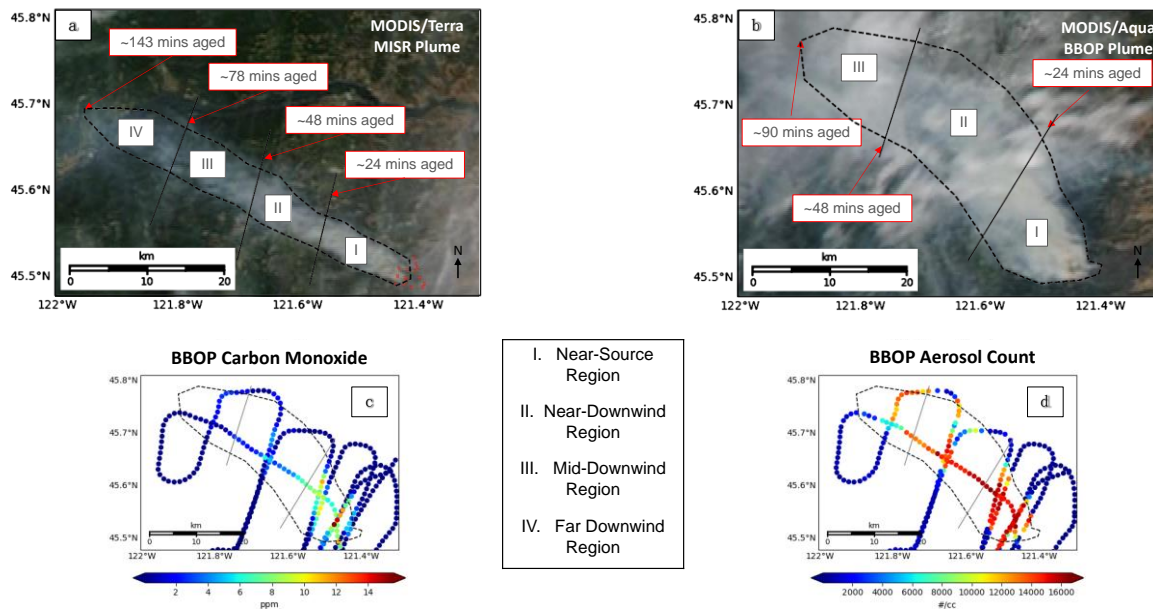


Figure 1. The Government Flats Complex Fire as seen on 21 August 2013: (a) at MISR overpass time (19:07 UTC; Moderate Resolution Imaging Spectroradiometer (MODIS) Terra red–green–blue (RGB) context image), and (b) during the Department of Energy’s Biomass Burning Observation Project (BBOP) flight operations (20:49 UTC; MODIS Aqua RGB image; the aircraft flight began at 21:20 UTC). The red dots in Panel (a) indicate MODIS-identified hot spots, which are used to estimate source location. The dashed lines represent the plume outlines we use for analysis. At both observation times, the plume is divided into regions (I–IV) based on estimated plume age, to allow for easy, qualitative comparison of inter- and intra-plume properties. Panels (c) and (d) represent the aircraft in situ CO and total aerosol count measurements, respectively.

3.1. In Situ Observations: A First Look

We provide an overview of the aircraft observations first, with an emphasis on the differences in smoke properties between regions. Figures 2 and 3 illustrate, as latitude/longitude plots, the chemical, optical, and physical properties, measured using the methods described in Section 2.3. Each point represents the aggregated ~1.1-km median value of a given measurement (except for Figure 2c, which did not need to be aggregated, as discussed in Section 2.3.3). Table 4 quantifies the mean, standard deviation (SD or σ), and median values of the measurements from Figures 2 and 3 for each region, and a comprehensive discussion of these statistics can be found in the Supplementary Materials.

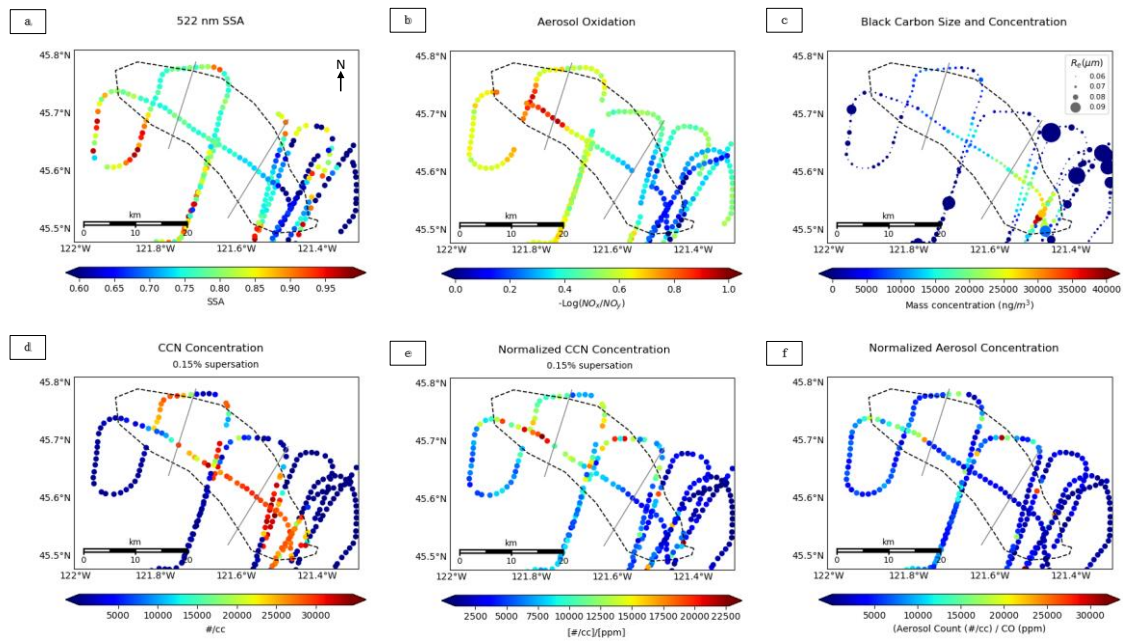


Figure 2. BBOP aircraft observations of the Government Flats Complex fire on 21 August 2013: (a) 522-nm SSA (particle soot absorption photometer (PSAP)/nepht); (b) aerosol oxidation (derived from the three-channel Oxides of Nitrogen Analyzer); (c) mass concentration of black carbon (BC) and size of BC-containing particles (single-particle soot photometer (SP2)); (d) concentration of particles that can act as cloud-condensation nuclei (CCN) at 0.15% supersaturation (CCN-200 instrument); (e) the CCN concentration divided by the CO concentration; (f) the total aerosol concentration divided by the CO concentration.

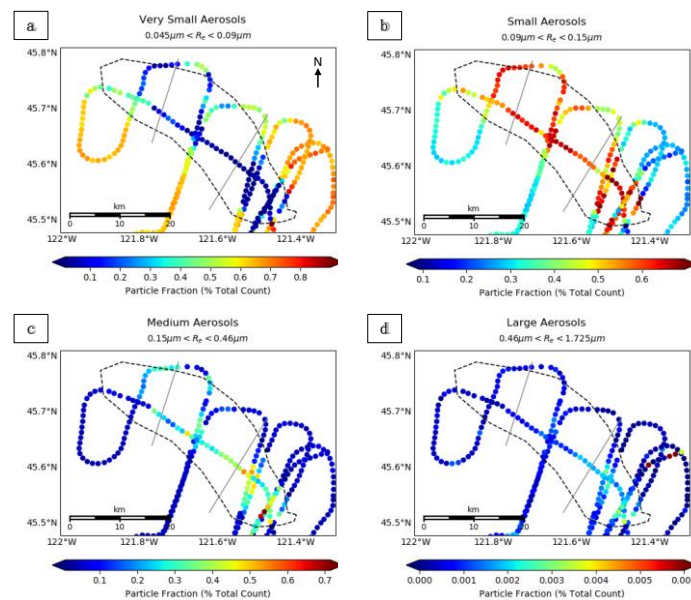


Figure 3. Fractional contributions (from zero to one) to the total aerosol count for (a) very small, (b) small, (c) medium, and (d) large aerosols in the Government Flats Complex Fire, as measured by the PCASP and CAS in situ instruments on 21 August 2013. The gray lines represent the boundaries between regions defined in Figure 1. Note: approximate size ranges are given above each plot, and the scales differ between categories.

Table 4. Aircraft data: aerosol size, chemical, and physical properties for the Government Flats Complex Fire measured in situ.

Plume Region:		Near-Source (I)	Near-Downwind (II)	Mid-Downwind (III)
Very small aerosols ^a	mean ± σ	0.1250 ± 0.1712	0.1904 ± 0.1626	0.2935 ± 0.1573
	median	0.03893	0.1121	0.3473
Small aerosols ^a	mean ± σ	0.5662 ± 0.1124	0.5930 ± 0.07029	0.5609 ± 0.1124
	median	0.5962	0.6096	0.5612
Medium aerosols ^a	mean ± σ	0.3072 ± 0.1534	0.2157 ± 0.1144	0.1452 ± 0.09571
	median	0.3072	0.2383	0.09315
Large aerosols ^a	mean ± σ	0.001549 ± 0.0007137	0.0008949 ± 0.0004193	0.0004482 ± 0.0002103
	median	0.001502	0.0008090	0.0004333
SSA ₅₂₂ ^b	mean ± σ	0.7001 ± 0.07297	0.7679 ± 0.030083	0.7814 ± 0.03647
	median	0.7029	0.7605	0.7748
Oxidation ^c	mean ± σ	0.2018 ± 0.1447	0.5307 ± 0.1400	0.7855 ± 0.1115
	median	0.2037	0.5318	0.8026
rBC mass ^d	mean ± σ	16,383.15 ± 8494.77	8638.98 ± 5765.73	4805.65 ± 3553.27
	median	17,437.12	8164.26	4036.97
rBC mass normalized by CO ^e	mean ± σ	8328.4 ± 15,678	5973.7 ± 10,509	4528.1 ± 4298.5
	median	2812.2	3388.7	3416.7
R _{e(BC)} ^f	mean ± σ	0.070 ± 0.0064	0.065 ± 0.0049	0.064 ± 0.0060
	median	0.070	0.065	0.065
CCN ₁₅ ^g	mean ± σ	24,273.13 ± 9852.24	19,976.24 ± 11,071.74	15,497.54 ± 10,310.76
	median	27,578.10	24,810.73	12,212.83
CCN ₁₅ normalized by CO ^h	mean ± σ	5710.84 ± 3566.64	10,657.30 ± 4390.24	14,829.78 ± 4112.40
	median	4716.05	9408.83	13,340.70
Aerosol count normalized by CO ⁱ	mean ± σ	3844.60 ± 4960.87	7048.10 ± 5861.56	9465.11 ± 5191.19
	median	2328.85	5015.14	7451.74
BrC absorption normalized by CO ^j	mean	172.39	216.97	207.14
	median	163.66	210.10	217.69
355-nm scattering normalized by CO ^k	mean	1771.90	2447.76	2515.30
	median	1591.90	2363.77	2377.25

^a Fraction of total aerosol count, as measured by the PCASP and CAS instruments in accordance with Table 3; ^b As measured by the PSAP/neph; ^c Defined as $-\log[\text{NO}_x/\text{NO}_y]$, using measurements provided by the three-channel Oxides of Nitrogen Analyzer, where 0 is fresh smoke and 1 is aged smoke; ^d As measured by the SP2, in ng/m^3 ; ^e The ratio of BC mass concentration (ng/m^3) and CO (ppm); ^f As measured by the SP2, in terms of effective radius R_e in μm ; ^g The concentration (#/cc) of CCN that activated at 0.15% supersaturation, as measured by the CCN-200; ^h The ratio of CCN₁₅ measured by the CCN-200 instrument (#/cc) and CO concentration measured by the Los Gatos Integrated Cavity Output Spectroscopy (ICOS) Analyzer (ppm); ⁱ The ratio of the total aerosol count from the PCASP/CAS instruments (#/cc) and the CO concentration measured by the Los Gatos ICOS Analyzer (ppm); ^j The residual of the ratio of 355-nm absorption (PAS; Mm^{-1}) and CO concentration (Los Gatos ICOS Analyzer; ppm) and the ratio of 522-nm absorption (PTI; Mm^{-1}) and CO concentration (Los Gatos ICOS Analyzer; ppm). Note that values only reflect data from the one along-plume transect. Standard deviations are not given as values were calculated by subtracting mean BC absorption from mean BrC absorption, rather than by the means of the residuals; ^k The ratio of 355-nm scattering (PAS; Mm^{-1}) and CO concentration (Los Gatos ICOS Analyzer; ppm). Note that values only reflect data from the one along-plume transect. Standard deviations are not given as values were calculated by subtracting mean BC absorption from mean BrC absorption, rather than by the means of the residuals.

In general, the plume contains fresh, highly absorbing smoke near the source that becomes both increasingly bright (SSA₅₂₂) and oxidized ($-\log[\text{NO}_x/\text{NO}_y]$) with downwind distance (Figure 2a,b, respectively). Both absolute and mean CO-normalized BC mass concentration decrease along the length of the plume (Figure 2c, Table 4); however, rates of BC dilution vary between the plume center (no increasing dilution with downwind distance) and the plume edges (increasing dilution with downwind distance). The disparities between the median and mean values in Table 4, as well as the differences in sampling seen in Figure 2, illustrate this pattern. CO-normalized CCN and aerosol concentration both increase along the length of the plume, particularly in the southern flank of region III, where smoke is the most oxidized (Figure 2e–f). CAS and PCASP data indicate the plume is comprised almost entirely of particles with r_e of 0.46 μm or less (i.e., “very small,” “small,” and “medium” particles, similar to

the aerosols of the same name identified within the MISR retrieval sensitivity limitations, discussed in Section 2.2 above). “Large” aerosols ($0.46 \mu\text{m} < r_e < 1.7 \mu\text{m}$) are essentially absent, never representing more than 0.35% of all particles, which is substantially below MISR retrieval sensitivity. Aerosol size decreases along the central plume transect, with the most dramatic decrease seen in the southern flank of region III (Figure 3). PTI (532 nm) and PAS (355 nm) absorption measurements used to distinguish spectrally flat from spectrally steep aerosols show that BC-only absorption (which is approximately equal at both wavelengths) declines more dramatically downwind than BrC-only absorption (the residual of 355-nm absorption minus 532-nm absorption), and that CO-normalized BrC absorption and CO-normalized 355-nm scattering actually increase dramatically in region II (Table 4). In their final campaign report, Kleinman and Sedlacek [18] also found that CO-normalized BrC absorption and scattering increased after ~30 min of plume aging. Although particle size is known to influence the spectral slope of SSA, the observed jump in 355-nm absorption and scattering does not correlate with significant changes in particle size, and thus it is likely that particle composition is the dominant factor driving the observed changes.

The in situ data alone do not provide enough information to fully explain these changes in aerosol properties. However, from available observations, we suggest several potential processes that could be affecting the plume particle properties: (1) *gravitational settling and/or dilution* that leads to the preferential decrease in medium-size particle concentration and BC particle concentration in regions II and III compared to region I; (2) *oxidation and/or SOA production*, leading to increased hygroscopicity and decreased light absorption contributions in regions II and III; (3) *changes in burning conditions at the source*, which alter the emitted smoke properties, reflected in particle-type differences between regions. Gravitational settling cannot be confirmed by the in situ data acquired at a single elevation. Particle oxidation state can be measured in situ, but can only be inferred from remote sensing, e.g., based on decreasing particle light absorption, although particle hydration is also possible, especially if particle size increases, hydrophilic particles (e.g., BrC) are present, and RH is high. If in situ measurements of particle size but not composition are available, the formation of secondary particles would have to be confirmed by total column measurements, as it is possible that decreases in particle size, as measured in situ, might instead be due to preferential gravitational settling of larger particles. However, the CO-normalized, absolute increase in small-particle concentration strongly supports the idea of particle formation in this case, as it indicates that dilution is minimal. Other particle evolution processes can occur, such as aggregation; however, based on the available in situ data, this does not seem likely here, unless it occurred very near source, where aerosol loading was extremely high. Changes in the burning conditions at the source cannot be confirmed or ruled out by remote sensing, and in situ measurements only allow us to infer the degree to which the fire may be changing. Several overlapping transects made by the BBOP aircraft at different times suggest measurements at a given distance from the source (i.e., similarly aged smoke at different times) are not dramatically different between these observations, indicating that changes in burning conditions may not be important here.

3.2. Satellite Observations: Validation and Providing a Broader Context

As demonstrated above, aircraft measurements provide highly detailed observations of the plume that allow us to identify general particle-type differences and to narrow down the list of potential aging mechanisms. However, the limited area sampled in situ across two hours, during which changes could have occurred, leaves us with an incomplete understanding of plume properties, and these data alone cannot resolve key uncertainties regarding the atmospheric particle processes that operated. Here, we provide an overview of the satellite observations, with the same emphasis on *differences* between regions as in Section 3.1, and we compare them with the aircraft measurements to assess the fidelity of the RA. We also demonstrate how the RA places in situ observations into a broader context, providing information critical for understanding the processes responsible for plume evolution.

Figure 4 contains standard MISR RA latitude/longitude plots of AOD, SSA, and ANG for the plume, with the MISR-MINX stereo heights included for reference. In addition to these, we map,

in terms of both retrieved absolute AOD and AOD fractional component, the spectral dependence of aerosol light absorption via the separate sums of (1) retrieved spectrally flat (BC analog) and (2) spectrally steep (BrC analog) light-absorbing components (Figure 5a–d), (3) the retrieved aerosol shape, via the non-spherical component LaNspHwab (Figure 5e–f), and (4) further information on absorption via the sum of all non-absorbing components (Figure 5g–h). These particle properties are, for the most part, neatly distinctive between the four plume regions, as discussed subsequently. It is important to reiterate that, when considering specific particle types (e.g., black carbon, brown carbon, dust, non-absorbing aerosols), the retrieved aerosol properties represent the optical equivalent of the aerosol present, i.e., the true aerosol is not necessarily a mixture of the specific components retrieved from among those in the RA climatology (e.g., Reference [30]). Table 5 quantifies the above-mentioned RA observations, giving the mean, standard deviation (SD or σ), and median for each region; a more in-depth analysis of these statistics can be found in the Supplementary Materials.

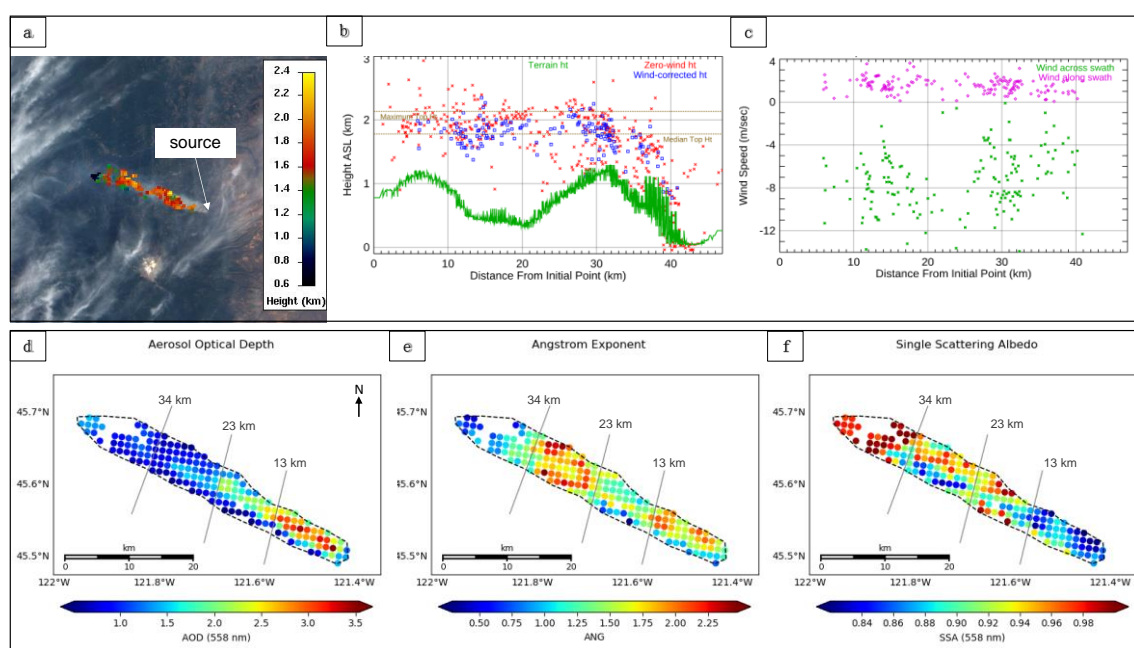


Figure 4. Plume properties for the Government Flats Complex Fire retrieved by MISR at 19:07 UTC (Orbit 72746, Path 45, Block 54) on 21 August 2013: (a) MISR Interactive Explorer (MINX) stereo height retrieval map; (b) MINX stereo height profile as a function of distance from the source, for both zero-wind (red) and wind-corrected (blue) analyses, with surface elevation indicated in green, (c) MINX-retrieved across-swath and along-swath wind vectors, and RA-derived (d) AOD at 558 nm, (e) extinction ANG, and (f) SSA at 558 nm. The transects for estimated plume ages corresponding to the regional boundaries in Figure 1 are indicated with thin gray lines in panels d–f.

The MISR–MINX stereo heights indicate the plume is concentrated mostly within 2 km above sea level (ASL), with a median height of 1.78 km and a maximum height of 2.13 km (Figure 4a–b). The RA-retrieved particle properties indicate peak AOD of up to 3.5 near the source, decreasing with downwind distance to a minimum of ~ 0.5 in some pixels within the area we defined as the observable plume in the satellite imagery (Figure 4d). The plume REPA also decreases significantly with downwind distance, and SSA increases from < 0.84 near the source to nearly 1.0 in region IV. Although most particles can be considered fine mode, having $ANG > 1$, REPS increases slightly in region II, dramatically decreases in region III, and then dramatically increases again in region IV (some pixels having $ANG < 1$), indicating significant changes in particle size throughout the length of the plume. Component analysis suggests that smoke near the source is largely a BC-like mixture, but that subsequent regions transition to mixtures interpreted as mostly non-absorbing and BC particles in

region II, then non-absorbing, BC, and BrC particles in region III, and non-absorbing and dust- or soil-like optical analogues in region IV (Figure 5). Bear in mind that these retrieved component AOD values and fractions represent an interpretation of the MISR column-integrated reflectances in terms of the components included in the RA (Table 2), whereas the REPS and REPA are less dependent on algorithm assumptions. This is one reason why validation with the in situ data is so important.

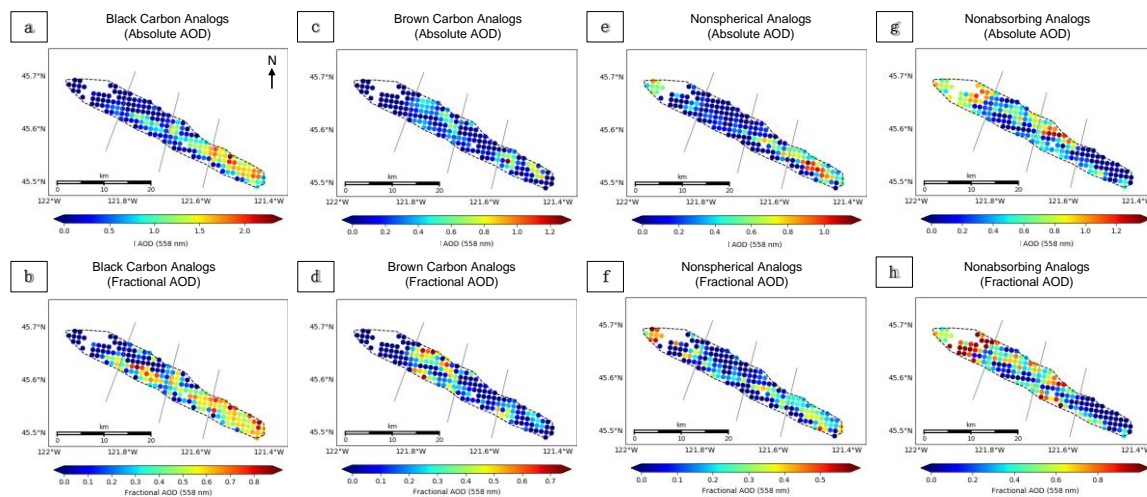


Figure 5. The absolute and fractional AOD of various MISR components for the Government Flats Complex Fire on 21 August 2013, where (a,b) are the sum of all “flat,” i.e., BC-like components, (c,d) are the sum of all “steep,” i.e., BrC-like components, (e,f) are the non-spherical dust-like components, and (g,h) are the sum of all non-light-absorbing components.

Table 5. MISR-observed particle properties for the Government Flats Complex Fire. AOD— aerosol optical depth; ANG—Ångström exponent.

Plume Region:		Near-Source (I)	Near-Downwind (II)	Mid-Downwind (III)	Far Downwind (IV)
AOD	mean \pm σ	2.222 \pm 0.7840	1.556 \pm 0.6195	0.9851 \pm 0.2856	1.020 \pm 0.2164
	median	2.281	1.653	0.8913	1.007
ANG	mean \pm σ	1.541 \pm 0.3800	1.319 \pm 0.3234	1.824 \pm 0.3106	1.042 \pm 0.3272
	median	1.583	1.293	1.822	1.024
SSA	mean \pm σ	0.8641 \pm 0.02926	0.9251 \pm 0.03960	0.9154 \pm 0.04117	0.9688 \pm 0.03889
	median	0.8639	0.9217	0.9229	0.9802
BC ^{a,b}	mean \pm σ	0.5606 \pm 0.1681	0.3649 \pm 0.2186	0.2727 \pm 0.2546	0.09674 \pm 0.1661
	median	0.5852	0.4156	0.2403	0
BrC ^{a,c}	mean \pm σ	0.1260 \pm 0.1304	0.08067 \pm 0.1106	0.3024 \pm 0.2102	0.02564 \pm 0.08594
	median	0.08545	0.03358	0.3049	0
Non-absorbing ^{a,d}	mean \pm σ	0.1069 \pm 0.1726	0.4434 \pm 0.2915	0.3498 \pm 0.2547	0.6914 \pm 0.2948
	median	0	0.4440	0.3835	0.7383
Non-spherical ^{a,e}	mean \pm σ	0.2064 \pm 0.1307	0.1110 \pm 0.1253	0.07516 \pm 0.09498	0.1863 \pm 0.1984
	median	0.2119	0.05470	0.0158	0.08771

^a In terms of fraction of total AOD (0 to 1); ^b The combined total all spectrally flat components, which are meant to represent black carbon; ^c The combined total of all spectrally steep components, which are meant to represent brown carbon; ^d The combined total of all non-absorbing components; ^e The only non-spherical component, meant to represent dust or soil.

The satellite and in situ measurements are substantially similar in their characterization of particle property evolution as a function of smoke age. In both cases, particle absorption systematically decreases downwind, accompanied by a transition from BC to BrC particle-type analogues as the dominant light-absorbing aerosol. Significantly smaller particles appear in region III and partway into region IV, between 48 and 90 min of aging. However, the MISR-retrieved particle sizes for smoke

between 24 and 48 min in age (region II) are larger than those near the source (although still fine-mode), whereas the aircraft observes the opposite trend. Moreover, unlike the aircraft measurements, MISR indicates that particles in region III are “small” in size, whereas the aircraft measures “very small” particles (Table 3). Lastly, MISR coverage continues past 90 min in age, observing region IV, where the retrieval results indicate particles eventually appear somewhat coarser in size and significantly non-spherical. Despite these differences, both observation sets indicate that, overall, from the source until ~78 min of aging, most of the plume comprises a majority of small, very small, and medium particles, with monotonically decreasing light absorption downwind.

Due to the comprehensive coverage, the MISR observations provide greater context for assessing the aerosol aging mechanisms that are suggested by the in situ data analysis. In region II, the increased REPS is in contrast with the decrease in particle size observed in situ. This may be explained by the difference in vertical sampling, as the aircraft measures at a single altitude, whereas the satellite observes the entire column. Column aerosol loading is dominated by the smoke plume in this case, but the plume is at least 0.75 km thick (Figure 4b); thus, measurements at a single elevation might not be representative. This would bolster the idea that gravitational settling is playing a role in this region. It is also possible that particle hydration, condensation of gaseous components onto existing particles, and/or particle aggregation are acting to increase particle size. The observed increase in relative humidity in this region (see Supplementary Materials, Figure S2) points toward hydration in particular, and the smaller sizes observed by the aircraft can be explained by differences in horizontal and possibly also vertical sampling. Aerosol oxidation is also acting in this region, as indicated by the increased oxidation values seen in Figure 2b and supported by the increased hygroscopicity seen in Figure 2e, as well as the decreased REPA in the MISR retrievals (Figure 4f).

In region III, there is strong in situ evidence for high levels of aerosol oxidation, leading to the formation of BrC either from SOA production (via the nucleation of new particles) or from the deposition of organic material onto BC particles, increasing hygroscopicity and decreasing light absorption. The aircraft does not observe strong changes in particle light absorption, as would be expected with these processes, although this could be due to limited sampling (Figure 2a). MISR does appear to see the expected increase in SSA (Figure 4f), at least along the northern part of the plume in this region. The main particle-type feature of region III is the dramatic decrease in REPS, accompanied by a decrease in total-column AOD. It is unclear from the limited in situ sampling (Figure 3c) whether medium particles are actually lost from the column here. However, region III begins about 30 km downwind of the source, and the MISR stereo height profile indicates that the plume descends toward the surface at about this distance (Figure 4b), suggesting selective, large-particle deposition is possible. This is supported by a decrease in the total-column AOD for medium-sized particles between regions II and III (Figure S3, Supplementary Materials). In addition, both absolute and fractional increases in small aerosol AOD are observed, strongly suggesting the formation of new particles. The dramatic increase in the CO-normalized aerosol concentrations in the aircraft data further supports this conclusion, as does the increase in both the absolute and the fractional BrC AOD observed by MISR. The formation of weakly absorbing organic aerosols (BrC) would also explain why SSA does not change more dramatically in this region.

Although the aircraft did not observe region IV, MISR points to potential aging mechanisms occurring here as well. Most notably, there is an increase in REPS, accompanied by decreasing MINX plume heights. Both the absolute and the fractional AOD of large and medium aerosols increase, suggesting that not only do small and very small particles disappear, but medium and large particles are being added (Figure S3, Supplementary Materials). At such a long downwind distance and with low overall AOD (Figure 4d), it is unlikely that particle aggregation is occurring in this region. Particle hydration might be involved, although the increase in non-spherical particles is not likely explained by this. Rather, these retrieval results might be due to a lack of larger, spherical, weakly absorbing particles in the aerosol climatology included in the MISR algorithm (Table 2), and, from a single satellite snapshot, we cannot rule out temporal changes at the smoke source.

3.3. Brief Summary of the Government Flats Smoke Plume Analysis

Overall, the satellite-retrieved particle properties are relatively well supported by the in situ observations, with minor disparities that can be explained by measurement uncertainty and sampling differences. Together, the data indicate that (1) there is a near-source region of high AOD with a mixture of dark, mostly spherical, small-medium particles, with light absorption dominated by BC, (2) there is an adjacent region downwind with reduced AOD comprising brighter, slightly larger particles that are less BC-like, (3) there is a subsequent downwind region where AOD is reduced further, with significantly smaller particles that are brighter in nature and akin to BrC, and (4) there is a region at the nominal end of the plume with relatively low AOD, high SSA, and a significant fraction of larger, possibly non-spherical particles.

Our interpretation of the RA results parallels the atmospheric–aerosol interactions suggested by the in situ data. Through column-integrated particle-type retrievals and plume stereo heights, the preferential gravitational settling of larger particles is supported in regions II and III. Furthermore, decreased REPA throughout the length of the plume bolsters the idea of particle oxidation and/or hydration in regions II and III. Lastly, a sharp decrease in REPS in region III accompanied by a dramatic increase in BrC particle AOD strongly supports the idea of new-particle SOA formation here, although the RA results alone cannot rule out condensation of gaseous compounds onto existing particles.

3.4. Secondary Comparisons: Using Non-Coincident RA and In Situ Observations

In the previous section, we investigated the effectiveness of the MISR RA as a tool for retrieving BB smoke particle properties, using near-coincident in situ data for validation. We also demonstrated how the RA can go further in describing plume particle properties by providing critical context for the aircraft observations. Here, we briefly summarize the results obtained by comparing MISR retrievals with BBOP data from two flights ~1 day prior to and ~1 day after the satellite overpass. This builds upon the results shown in the previous sections and allows us to explore the utility of the RA for characterizing non-coincident observations (more complete results for these two cases are given in the Supplementary Materials). The observed differences between the datasets illustrate the variable nature of BB plume dynamics and particle properties on time scales longer than a few hours, and they further highlight the value of combining satellite and in situ observations where possible to understand plume development more deeply. As such, combining multiple particle property observations, with different sensitivities and under different conditions, as well as with different spatial resolutions and coverage, creates a more complete picture of plume composition and evolution. Below are highlights from these comparisons, and we present detailed written and graphical analyses in the Supplementary Materials (Figures S4–S10 for the Colockum Tarps Fire and Figures S11–S17 for the Douglas Complex Fire).

3.4.1. The Colockum Tarps Fire: Aircraft Observations Preceding Satellite Observations

The Colockum Tarps Fire, first ignited due to human causes, burned from 25 July 2013 through 15 August 2013 in southern central Washington [64]. The 26 July 2013 BBOP research flight and the subsequent 27 July MISR overpass observed the resulting smoke plume. Taken together, the satellite and in situ observations describe a plume with fine-mode, highly absorbing particles near the source that become brighter downwind, although the MISR RA observes slightly smaller particles overall than the CAS and PCASP data. From the available data, the main inferences we draw about particle evolution in the Colockum Tarps Fire plumes are that the near-source aerosols tend to be smaller and more light-absorbing than downwind. Plume dilution seems to be independent of particle size, as MISR-retrieved effective particle size (REPS) does not decrease systematically downwind, and the aircraft CO-normalized aerosol concentration does not change significantly either. Aerosol oxidation is a factor in aging based on the in situ data and is likely also the explanation for a downwind increase in particle SSA observed by MISR the following day. Unlike the Government Flats fire plume, on both days, the Colockum Tarps plume retains areas of high BC fraction over the entire plume extent.

As particle properties vary non-uniformly with distance from the source on length scales under 10 km in this plume, it seems likely that the primary smoke emissions from this fire varied on time scales shorter than an hour.

3.4.2. The Douglas Complex Fire: Satellite Observations Preceding Aircraft Observations

The Douglas Complex fire was a large system originally comprised of dozens of lightning-sparked fires that ignited on 26 July 2013 and burned through 19 August 2013 in southern coastal Oregon [63]. The 5 August 2013 MISR overpass and the subsequent 6 August BBOP research flight observed the smoke plumes that were produced. The combined information from the satellite and aircraft data suggest small–medium particle sizes in the thickest parts of the plume and very small or small particles in the surrounding smoke, although the RA retrieves overall slightly larger particles than the aircraft data on the previous day, and also finds a significant AOD contribution from large particles in the plume core. Particles near the source are moderately light-absorbing as seen by MISR, but are brighter the next day during aircraft flight operations, when the fire appears to be a bit more active in the imagery. The horizontal structure of this plume suggests that the smoke observed here is stagnant, having piled up and just spread out locally due to low wind speeds, while undergoing atmospheric processing. This is supported by the presence of larger particle sizes in the core on both days, as piled-up smoke could facilitate particle coagulation, condensation that leads to deposition of coatings on existing particles, and possibly particle hydration from fire-generated water vapor in a cooling plume. The increased CO-normalized CCN and aerosol concentrations outside the core region suggest possible SOA formation via the nucleation of new particles in the surroundings, where the fraction of very small particles is higher.

4. Conclusions

The BBOP data allow us to explore the strengths and limitations of the satellite data for characterizing wildfire smoke plume extent and particle properties. Where near-coincident data were acquired, the MISR-retrieved particle properties and those measured in situ are similar, showing consistent spatial patterns, with measurement uncertainty and sampling differences easily accounting for the observed differences. The results also demonstrate smoke-plume evolution generally consistent with previous modeling studies (e.g., References [65,66]), but providing extensive observations of a number of key smoke-plume properties not previously obtained from remote-sensing; these could be used to refine modeling options for different types of fires, globally. For the three cases analyzed here, the satellite and in situ data both captured the similarities and differences in plume structure, the relationships between denser, near-source smoke and more oxidized, less light-absorbing particles downwind, and the scales over which these transitions occurred. Furthermore, despite some limitations, the use of the MISR RA in conjunction with non-coincident in situ measurements allows for a more comprehensive analysis of plume particle properties and presents a method for studying particle aging on larger spatial and longer temporal scales, where satellite coverage is acquired but aircraft data are lacking.

The in situ data offer chemical and microphysical detail, such as the degree of particle oxidation and the specific distribution of particle sizes, as well as particle concentrations, which cannot be obtained from available satellite observations. However, the satellite snapshots offer maps of qualitative particle properties and extensive coverage, which sometimes capture aspects of the plume missed by the aircraft transects. For example, differences in plume structure among the three cases presented here were captured most effectively by the whole-plume MISR observations: the systematic change in AOD and particle properties along the length of the Government Flats plume, the patchy and more variable particle property distribution along the Colockum Tarps plume, and the seemingly stagnant pile-up of smoke particles for the Douglas Complex plume. As such, the satellite data provide the context needed to derive relationships among plume elements of different ages, making it possible to

infer attributes of plume-particle evolution. Furthermore, MISR has obtained global coverage about once per week for over 20 years, providing a vast trove of smoke-plume observations for further study.

Future work will involve applying MISR plume height and particle property retrievals to a wide variety of cases that are less well constrained by other observations. Statistical analysis of plume particle properties from a range of BB events, focusing on the apparent changes in particle size, SSA, and SSA spectral dependence, should improve our understanding of different sources, as well as of different aging mechanisms within and between smoke plumes. Such insight represents new territory in aerosol studies and can contribute to improving climate and air quality modeling.

Supplementary Materials: The following are available online at <http://www.mdpi.com/2072-4292/12/5/769/s1>: Figure S1: Government Flats MISR-MINX wind vectors; Figure S2: Aircraft-observed relative humidity for the Government Flats Complex Fire; Figure S3: MISR-observed particle sizes for the Government Flats Complex Fire; Figure S4: Aircraft and satellite views of the Colockum Tarps Fire; Figure S5: Aircraft chemical and radiative observations from the Colockum Tarps Fire; Figure S6: Aircraft-observed particle sizes for the Colockum Tarps Fire; Figure S7: Aircraft-observed black carbon particle size for the Colockum Tarps Fire; Figure S8: MISR-observed plume heights and particle properties for the Colockum Tarps Fire; Figure S9: MISR-observed particle sizes for the Colockum Tarps Fire; Figure S10: MISR-observed particle types for the Colockum Tarps Fire; Figure S11: Aircraft and satellite views of the Douglas Complex Fire; Figure S12: MISR-observed plume heights and particle properties for the Douglas Complex Fire; Figure S13: MISR-observed particle sizes for the Douglas Complex Fire; Figure S14: MISR-observed particle types for the Douglas Complex Fire; Figure S15: Aircraft chemical and radiative observations from the Douglas Complex Fire; Figure S16: Aircraft-observed particle sizes for the Douglas Complex Fire; Figure S7: Aircraft-observed black carbon particle size for the Douglas Complex Fire. Text providing detailed analysis of the Government Flats, Colockum Tarps, and Douglas Complex fire plumes is included in the Supplement, along with the figures.

Author Contributions: The project was first conceptualized by R.K., and the development and design of the methodology were a collaboration between R.K. and K.J.N. The RA algorithm used in this project was developed by R.K. and J.L., and is supported by J.L., K.J.N. developed the tools used to analyze and visualize the results of both the RA and in situ data. Formal analysis of results was conducted by K.J.N. and R.K., who together wrote the original draft. Reviewing and editing were conducted by A.S., Z.L., and L.K., R.K. also provided supervision and project administration. All authors read and agreed to the published version of the manuscript.

Funding: The work of K.T. Junghenn Noyes is supported in part by a grant from the Maryland Space Grant Consortium under Richard C. Henry and Matt Collinge. The work of R.A. Kahn and J.A. Limbacher is supported in part by NASA's Climate and Radiation Research and Analysis Program under Hal Maring, NASA's Atmospheric Composition Program under Richard Eckman, and the EOS Terra Project under Kurtis Thome. The work of Z. Li is supported by a NASA grant (NNX16AN61G). K.T. Junghenn Noyes also receives partial support from the programs that cover R. Kahn and Z. Li. L.I. Kleinman and A.J. Sedlacek III were supported through the US DOE Office of Biological and Environmental Sciences (OBER) Atmospheric Research Program (ASR) under contract DE-SC0012704 (BNL).

Acknowledgments: The authors recognize the DOE Atmospheric Radiation Measurement (ARM) Climate Research program and facility for both the support to carry out the BBOP campaign and the use of the G-1 research aircraft. We also thank the BBOP instrument PI's Fan Mei (CCN counter, Pacific Northwest National Laboratory), Duli Chand (PSAP and nephelometer, Pacific Northwest National Laboratory), William Arnott (PAS, University of Nevada Reno), Jason Tomlinson, (CAS and PCASP, Pacific Northwest National Laboratory), and Stephen Springston (trace gas instrument suite, Brookhaven National Laboratory). Arthur Sedlacek was responsible for the SP2 data. We further acknowledge Bob Yokelson (University of Montana) for helpful discussions on fire chemistry, G. Thomas Arnold (NASA Goddard Space Flight Center) for assistance with image processing, and Jaewha Lee (NASA Goddard Space Flight Center) for helpful information on the use of his non-spherical particle optical model.

Conflicts of Interest: The authors declare no conflicts of interest.

References

1. Colarco, P.R.; Schoeberl, M.R.; Doddridge, B.G.; Marufu, L.T.; Torres, O.; Welton, E.J. Transport of Smoke from Canadian Forest Fires to the Surface near Washington, D.C.: Injection Height, Entrainment, and Optical Properties. *J. Geophys. Res.* **2004**, *109*. [[CrossRef](#)]
2. Kahn, R.A.; Chen, Y.; Nelson, D.L.; Leung, F.-Y.; Li, Q.; Diner, D.J.; Logan, J.A. Wildfire Smoke Injection Heights: Two Perspectives from Space. *Geophys. Res. Lett.* **2008**, *35*, L04809. [[CrossRef](#)]

3. Warner, J.; Twomey, S. The Production of Cloud Nuclei by Cane Fires and the Effect on Cloud Droplet Concentration. *J. Atmos. Sci.* **1967**, *24*, 704–706. [[CrossRef](#)]
4. Hobbs, P.V.; Radke, L.F. Cloud Condensation Nuclei from a Simulated Forest Fire. *Science* **1969**, *163*, 279–280. [[CrossRef](#)]
5. Kaufman, Y.J.; Fraser, R.S. The Effect of Smoke Particles on Clouds and Climate Forcing. *Science* **1997**, *277*, 1636–1639. [[CrossRef](#)]
6. Albrecht, B.A. Aerosols, Cloud Microphysics, and Fractional Cloudiness. *Science* **1989**, *245*, 1227–1230. [[CrossRef](#)]
7. Dubovik, O.; Holben, B.; Eck, T.F.; Smirnov, A.; Kaufman, Y.J.; King, M.D.; Tanre, D.; Slutsker, I. Variability of Absorption and Optical Properties of Key Aerosol Types Observed in Worldwide Locations. *J. Atmos. Sci.* **2002**, *59*, 19. [[CrossRef](#)]
8. Chen, W.-T.; Kahn, R.A.; Nelson, D.; Yau, K.; Seinfeld, J.H. Sensitivity of Multiangle Imaging to the Optical and Microphysical Properties of Biomass Burning Aerosols. *J. Geophys. Res.* **2008**, *113*, D10203. [[CrossRef](#)]
9. Eck, T.F.; Holben, B.N.; Reid, J.S.; O'Neill, N.T.; Schafer, J.S.; Dubovik, O.; Smirnov, A.; Yamasoe, M.A.; Artaxo, P. High Aerosol Optical Depth Biomass Burning Events: A Comparison of Optical Properties for Different Source Regions. *Geophys. Res. Lett.* **2003**, *30*. [[CrossRef](#)]
10. Shi, S.; Cheng, T.; Gu, X.; Guo, H.; Wu, Y.; Wang, Y. Biomass Burning Aerosol Characteristics for Different Vegetation Types in Different Aging Periods. *Environ. Int.* **2019**, *126*, 504–511. [[CrossRef](#)] [[PubMed](#)]
11. Chakrabarty, R.K.; Moosmüller, H.; Chen, L.-W.A.; Lewis, K.; Arnott, W.P.; Mazzoleni, C.; Dubey, M.K.; Wold, C.E.; Hao, W.M.; Kreidenweis, S.M. Brown Carbon in Tar Balls from Smoldering Biomass Combustion. *Atmos. Chem. Phys.* **2010**, *10*, 6363–6370. [[CrossRef](#)]
12. Chakrabarty, R.K.; Gyawali, M.; Yatavelli, R.L.N.; Pandey, A.; Watts, A.C.; Knue, J.; Chen, L.-W.A.; Pattison, R.R.; Tsibert, A.; Samburova, V.; et al. Brown Carbon Aerosols from Burning of Boreal Peatlands: Microphysical Properties, Emission Factors, and Implications for Direct Radiative Forcing. *Atmos. Chem. Phys.* **2016**, *16*, 3033–3040. [[CrossRef](#)]
13. Petrenko, M.; Kahn, R.; Chin, M.; Soja, A.; Kucsera, T.; Harshvardhan. The Use of Satellite-Measured Aerosol Optical Depth to Constrain Biomass Burning Emissions Source Strength in the Global Model GOCART. *J. Geophys. Res.* **2012**, *117*. [[CrossRef](#)]
14. Samset, B.H.; Stjern, C.W.; Andrews, E.; Kahn, R.A.; Myhre, G.; Schulz, M.; Schuster, G.L. Aerosol Absorption: Progress Towards Global and Regional Constraints. *Curr. Clim. Chang. Rep.* **2018**, *4*, 65–83. [[CrossRef](#)] [[PubMed](#)]
15. Akagi, S.K.; Craven, J.S.; Taylor, J.W.; McMeeking, G.R.; Yokelson, R.J.; Burling, I.R.; Urbanski, S.P.; Wold, C.E.; Seinfeld, J.H.; Coe, H.; et al. Evolution of Trace Gases and Particles Emitted by a Chaparral Fire in California. *Atmos. Chem. Phys.* **2012**, *12*, 1397–1421. [[CrossRef](#)]
16. Zhou, S.; Collier, S.; Jaffe, D.A.; Briggs, N.L.; Hee, J.; Sedlacek, A.J., III; Kleinman, L.; Onasch, T.B.; Zhang, Q. Regional Influence of Wildfires on Aerosol Chemistry in the Western US and Insights into Atmospheric Aging of Biomass Burning Organic Aerosol. *Atmos. Chem. Phys.* **2017**, *17*, 2477–2493. [[CrossRef](#)]
17. Kleinman, L.I.; Sedlacek, A.J. *Biomass Burning Observation Project Science Plan*; DOE/SC-ARM; Brookhaven National Laboratory (BNL): Upton, NY, USA, 2013.
18. Kleinman, L.I.; Sedlacek, A.J. *Biomass Burning Observation Project (BBOP): Final Campaign Report*; DOE ARM Climate Research Facility: Washington, DC, USA, 2016.
19. Toon, O.B.; Maring, H.; Dibb, J.; Ferrare, R.; Jacob, D.J.; Jensen, E.J.; Luo, Z.J.; Mace, G.G.; Pan, L.L.; Pfister, L.; et al. Planning, Implementation, and Scientific Goals of the Studies of Emissions and Atmospheric Composition, Clouds and Climate Coupling by Regional Surveys (SEAC⁴RS) Field Mission. *J. Geophys. Res. Atmos.* **2016**, *121*, 4967–5009. [[CrossRef](#)]
20. Forrister, H.; Liu, J.; Scheuer, E.; Dibb, J.; Ziemba, L.; Thornhill, K.L.; Anderson, B.; Diskin, G.; Perring, A.E.; Schwarz, J.P.; et al. Evolution of Brown Carbon in Wildfire Plumes. *Geophys. Res. Lett.* **2015**, *42*, 4623–4630. [[CrossRef](#)]
21. Sedlacek, A.J., III; Buseck, P.R.; Adachi, K.; Onasch, T.B.; Springston, S.R.; Kleinman, L. Formation and Evolution of Tar Balls from Northwestern US Wildfires. *Atmos. Chem. Phys.* **2018**, *18*, 11289–11301. [[CrossRef](#)]

22. Adachi, K.; Sedlacek, A.J.; Kleinman, L.; Springston, S.R.; Wang, J.; Chand, D.; Hubbe, J.M.; Shilling, J.E.; Onasch, T.B.; Kinase, T.; et al. Spherical Tarball Particles Form through Rapid Chemical and Physical Changes of Organic Matter in Biomass-Burning Smoke. *Proc. Natl. Acad. Sci. USA* **2019**, *116*, 19336–19341. [[CrossRef](#)]
23. Feng, Y.; Ramanathan, V.; Kotamarthi, V.R. Brown Carbon: A Significant Atmospheric Absorber of Solar Radiation? *Atmos. Chem. Phys.* **2013**, *13*, 8607–8621. [[CrossRef](#)]
24. Jethva, H.; Torres, O. Satellite-Based Evidence of Wavelength-Dependent Aerosol Absorption in Biomass Burning Smoke Inferred from Ozone Monitoring Instrument. *Atmos. Chem. Phys.* **2011**, *11*, 10541–10551. [[CrossRef](#)]
25. Konovalov, I.B.; Beekmann, M.; Berezin, E.V.; Formenti, P.; Andreae, M.O. Probing into the Aging Dynamics of Biomass Burning Aerosol by Using Satellite Measurements of Aerosol Optical Depth and Carbon Monoxide. *Atmos. Chem. Phys.* **2017**, *17*, 4513–4537. [[CrossRef](#)]
26. Kahn, R.A. A global perspective on wildfires. *EOS Am. Geophys. Union* **2020**, *101*. [[CrossRef](#)]
27. Nelson, D.; Garay, M.; Kahn, R.; Dunst, B. Stereoscopic Height and Wind Retrievals for Aerosol Plumes with the MISR INteractive EXplorer (MINX). *Remote Sens.* **2013**, *5*, 4593–4628. [[CrossRef](#)]
28. Limbacher, J.A.; Kahn, R.A. MISR Research-Aerosol-Algorithm Refinements for Dark Water Retrievals. *Atmos. Meas. Technol.* **2014**, *7*, 3989–4007. [[CrossRef](#)]
29. Limbacher, J.A.; Kahn, R.A. Updated MISR Over-Water Research Aerosol Retrieval Algorithm—Part 2: A Multi-Angle Aerosol Retrieval Algorithm for Shallow, Turbid, Oligotrophic, and Eutrophic Waters. *Atmos. Meas. Technol.* **2019**, *12*, 675–689. [[CrossRef](#)]
30. Kahn, R.A.; Limbacher, J. Eyjafjallajökull Volcano Plume Particle-Type Characterization from Space-Based Multi-Angle Imaging. *Atmos. Chem. Phys.* **2012**, *12*, 9459–9477. [[CrossRef](#)]
31. Scollo, S.; Kahn, R.A.; Nelson, D.L.; Coltelli, M.; Diner, D.J.; Garay, M.J.; Realmuto, V.J. MISR Observations of Etna Volcanic Plumes. *J. Geophys. Res.* **2012**, *117*. [[CrossRef](#)]
32. Flower, V.J.B.; Kahn, R.A. Distinguishing Remobilized Ash From Erupted Volcanic Plumes Using Space-Borne Multiangle Imaging: Remobilized Ash Plumes. *Geophys. Res. Lett.* **2017**, *44*, 10772–10779. [[CrossRef](#)]
33. Flower, V.J.B.; Kahn, R.A. Karymsky Volcano Eruptive Plume Properties Based on MISR Multi-Angle Imagery and the Volcanological Implications. *Atmos. Chem. Phys.* **2018**, *18*, 3903–3918. [[CrossRef](#)] [[PubMed](#)]
34. Flower, V.J.B.; Kahn, R.A. Interpreting the Volcanological Processes of Kamchatka, Based on Multi-Sensor Satellite Observations. *Remote Sens. Environ.* **2020**, *237*, 111585. [[CrossRef](#)]
35. Kahn, R.A.; Gaitley, B.J. An Analysis of Global Aerosol Type as Retrieved by MISR: MISR Aerosol Type. *J. Geophys. Res. Atmos.* **2015**, *120*, 4248–4281. [[CrossRef](#)]
36. Diner, D.J.; Beckert, J.C.; Reilly, T.H.; Bruegge, C.J.; Conel, J.E.; Kahn, R.A.; Martonchik, J.V.; Ackerman, T.P.; Davies, R.; Gerstl, S.A.W.; et al. Multi-Angle Imaging Spectroradiometer (MISR) Instrument Description and Experiment Overview. *IEEE Trans.* **1998**, *36*, 1072–1087. [[CrossRef](#)]
37. Nelson, D.L.; Chen, Y.; Kahn, R.A.; Diner, D.J.; Mazzoni, D. Example Applications of the MISR INteractive EXplorer (MINX) Software Tool to Wildfire Smoke Plume Analyses. *Remote Sens. Fire Sci. Appl.* **2008**, 708909. [[CrossRef](#)]
38. Val Martin, M.; Logan, J.A.; Kahn, R.A. Smoke Injection Heights from Fires in North America: Analysis of 5 Years of Satellite Observations. *Atmos. Chem. Phys.* **2010**, *10*, 1491–1510. [[CrossRef](#)]
39. Val Martin, M.; Kahn, R.; Tosca, M. A Global Analysis of Wildfire Smoke Injection Heights Derived from Space-Based Multi-Angle Imaging. *Remote Sens.* **2018**, *10*, 1609. [[CrossRef](#)]
40. Tosca, M.G.; Randerson, J.T.; Zender, C.S.; Nelson, D.L.; Diner, D.J.; Logan, J.A. Dynamics of Fire Plumes and Smoke Clouds Associated with Peat and Deforestation Fires in Indonesia. *J. Geophys. Res.* **2011**, *116*, D08207. [[CrossRef](#)]
41. Flower, V.J.B.; Kahn, R.A. Assessing the Altitude and Dispersion of Volcanic Plumes Using MISR Multi-Angle Imaging from Space: Sixteen Years of Volcanic Activity in the Kamchatka Peninsula, Russia. *J. Volcanol. Geoth. Res.* **2017**, *337*, 1–15. [[CrossRef](#)]
42. Yu, Y.; Kalashnikova, O.V.; Garay, M.J.; Lee, H.; Notaro, M. Identification and Characterization of Dust Source Regions Across North Africa and the Middle East Using MISR Satellite Observations. *Geophys. Res. Lett.* **2018**, *45*, 6690–6701. [[CrossRef](#)]
43. Vernon, C.J.; Bolt, R.; Canty, T.; Kahn, R.A. The Impact of MISR-Derived Injection Height Initialization on Wildfire and Volcanic Plume Dispersion in the HYSPLIT Model. *Atmos. Meas. Technol.* **2018**, *11*, 6289–6307. [[CrossRef](#)]

44. Kahn, R.A.; Gaitley, B.J.; Garay, M.J.; Diner, D.J.; Eck, T.; Smirnov, A.; Holben, B.N. Multiangle Imaging SpectroRadiometer global aerosol product assessment by comparison with the Aerosol Robotic Network. *J. Geophys. Res.* **2010**, *115*, D23209. [[CrossRef](#)]
45. Lee, J.; Hsu, N.C.; Sayer, A.M.; Bettenhausen, C.; Yang, P. AERONET-Based Nonspherical Dust Optical Models and Effects on the VIIRS Deep Blue/SOAR Over Water Aerosol Product: Dust Optical Models for Deep Blue/SOAR. *J. Geophys. Res. Atmos.* **2017**, *122*, 10384–10401. [[CrossRef](#)] [[PubMed](#)]
46. Andreae, M.O.; Gelencser, A. Black Carbon or Brown Carbon? The Nature of Light-Absorbing Carbonaceous Aerosols. *Atmos. Chem. Phys.* **2006**, *18*, 3419–3463. [[CrossRef](#)]
47. Lyapustin, A.; Wang, Y. *MODIS Multi-Angle Implementation of Atmospheric Correction (MAIAC) Data User's Guide*; NASA: Greenbelt, MD, USA, 2018.
48. Chand, D.; Schmid, B. Nephelometer PSAP, BBOP. Atmospheric Radiation Measurement Climate Research Facility. 2015. Available online: <https://www.osti.gov/biblio/1461871-nephelometer-psap-bbop> (accessed on 30 January 2020). [[CrossRef](#)]
49. Anderson, T.L.; Ogren, J.A. Determining Aerosol Radiative Properties Using the TSI 3563 Integrating Nephelometer. *Aerosol Sci. Technol.* **1998**, *29*, 57–69. [[CrossRef](#)]
50. Bond, T.C.; Anderson, T.L.; Campbell, D. Calibration and Intercomparison of Filter-Based Measurements of Visible Light Absorption by Aerosols. *Aerosol Sci. Technol.* **1999**, *30*, 582–600. [[CrossRef](#)]
51. Ogren, J.A. Comment on “Calibration and Intercomparison of Filter-Based Measurements of Visible Light Absorption by Aerosols”. *Aerosol Sci. Technol.* **2010**, *44*, 589–591. [[CrossRef](#)]
52. Springston, S.R. *Particle Soot Absorption Photometer (PSAP) Instrument Handbook*; DOE ARM Climate Research Facility: Washington, DC, USA, 2018.
53. Arnott, W.P. PAS, BBOP. Atmospheric Radiation Measurement Climate Research Facility. 2013. Available online: <https://adc.arm.gov/discovery/#v/results/s/s::bbop> (accessed on 20 December 2019).
54. Sedlacek, A.; Lee, J. Photothermal Interferometric Aerosol Absorption Spectrometry. *Aerosol Sci. Technol.* **2007**, *41*, 1089–1101. [[CrossRef](#)]
55. Reid, J.S.; Koppmann, R.; Eck, T.F.; Eleuterio, D.P. A Review of Biomass Burning Emissions Part II: Intensive Physical Properties of Biomass Burning Particles. *Atmos. Chem. Phys.* **2005**, *28*, 799–825. [[CrossRef](#)]
56. Uin, J. *Cloud Condensation Nuclei Particle Counter Instrument Handbook*; DOE ARM Climate Research Facility: Washington, DC, USA, 2016.
57. Mei, F. AAF-CCN, BBOP. Atmospheric Radiation Measurement Climate Research Facility. 2013. Available online: <https://adc.arm.gov/discovery/#v/results/s/s::bbop> (accessed on 20 September 2019).
58. Yokelson, R.J.; Crounse, J.D.; DeCarlo, P.F.; Karl, T.; Urbanski, S.; Atlas, E.; Campos, T.; Shinzuka, Y.; Kapustin, V.; Clarke, A.D.; et al. Emissions from Biomass Burning in the Yucatan. *Atmos. Chem. Phys.* **2009**, *28*, 5785. [[CrossRef](#)]
59. Kleinman, L.I.; Springston, S.R.; Daum, P.H.; Weinstein-Lloyd, J.; Alexander, M.L.; Hubbe, J.; Ortega, J.; Canagaratna, M.R.; Jayne, J. The Time Evolution of Aerosol Composition over the Mexico City Plateau. *Atmos. Chem. Phys.* **2008**, *17*, 14461–14509. [[CrossRef](#)]
60. DeCarlo, P.F.; Dunlea, E.J.; Kimmel, J.R.; Aiken, A.C.; Sueper, D.; Crounse, J.; Wennberg, P.O.; Emmons, L.; Shinzuka, Y.; Clarke, A.; et al. Fast Airborne Aerosol Size and Chemistry Measurements above Mexico City and Central Mexico during the MILAGRO Campaign. *Atmos. Chem. Phys.* **2008**, *8*, 4027–4048. [[CrossRef](#)]
61. Sedlacek, A.J. *Single Particle Soot Photometers (SP2) Instrument Handbook*; DOE ARM Climate Research Facility: Washington, DC, USA, 2017.
62. Sedlacek, A.J.; Lewis, E.R.; Kleinman, L.; Xu, J.; Zhang, Q. Determination of and Evidence for Non-Core-Shell Structure of Particles Containing Black Carbon Using the Single-Particle Soot Photometer (SP2). *Geophys. Res. Lett.* **2012**, *39*. [[CrossRef](#)]
63. Oregon Department of Forestry: Fires List. Available online: https://apps.odf.oregon.gov/DIVISIONS/protection/fire_protection/fires/FIREList.asp (accessed on 28 December 2019).
64. National Fire and Aviation Management: Incident Status Summary. Available online: https://fam.nwcg.gov/fam-web/hist_209/hist_r_print_209_head_2013?v_number=WA-SES-349&v_report_date=08/18/2013&v_hour=1200&v_gaid=NW (accessed on 28 December 2019).

65. Hodshire, A.L.; Bian, Q.; Ramnarine, E.; Lonsdale, C.R.; Alvarado, M.J.; Kreidenweis, S.M.; Jathar, S.H.; Pierce, J.R. More than emissions and chemistry: Fire size, dilution, and background aerosol also greatly influence near-field biomass burning aerosol aging. *J. Geophys. Res. Atmos.* **2019**, *124*, 5589–5611. [[CrossRef](#)]
66. Konovalov, I.B.; Beekmann, M.; Golovushkin, N.A.; Andreae, M.O. Nonlinear behavior of organic aerosol in biomass burning plumes: A microphysical model analysis. *Atmos. Chem. Phys.* **2019**, *19*, 12091–12119. [[CrossRef](#)]



© 2020 by the authors. Licensee MDPI, Basel, Switzerland. This article is an open access article distributed under the terms and conditions of the Creative Commons Attribution (CC BY) license (<http://creativecommons.org/licenses/by/4.0/>).

Supplementary Material, Part 1

We present in the first section of this supplement two figures that support the main text and are referenced in the discussion the Government Flats Complex Fire (Sections 3.1 and 3.2).

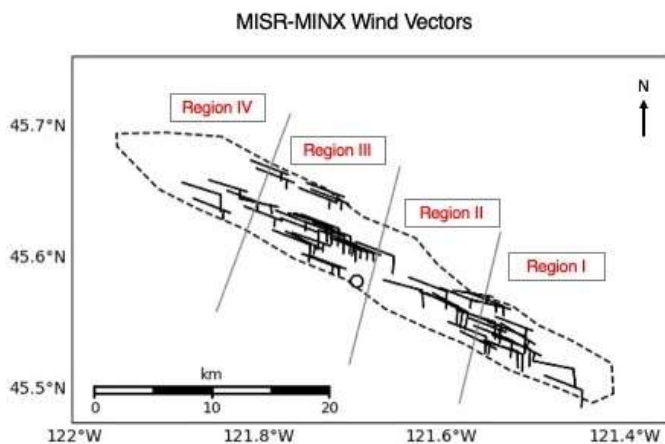


Figure S1. Wind trajectories retrieved from the MISR-MINX software tool (in units of knots) for the Government Flats Complex Fire. Half-barbs indicate 5 knots, full barbs are 10 knots. The grey lines represent the regional boundaries within the plume (See Fig. 1a). Empty circles are points where the retrieved wind speed was zero.

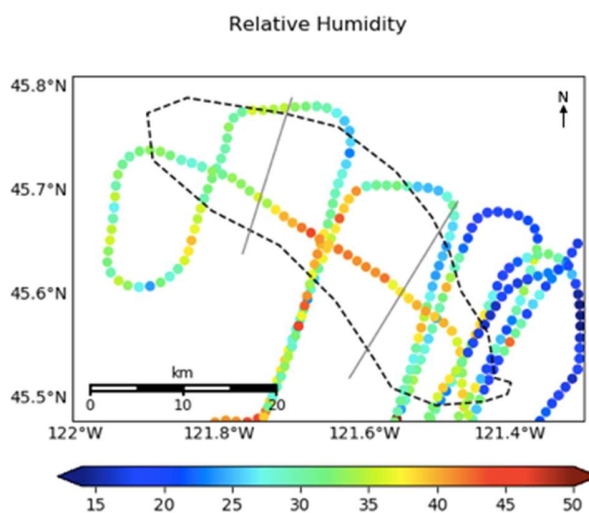


Figure S2. Percent relative humidity observed from the BBOP G-1 aircraft for the Government Flats Complex Fire.

Supplementary Material, Part 2

We present in the second section of this supplement detailed descriptions of the *in situ* and spacecraft observations collected for the Government Flats Complex Fire, by region. (This elaborates on Sections 3.1 and 3.2 in the main text.)

I. Aircraft *in situ* Observations of the Government Flats Complex Fire

As expected, the *in situ* observations indicate the highest CO and aerosol concentrations near the source, decreasing downwind. Virtually all points outside the plume boundaries contain fewer than 2,000 particles/cm³, as measured by the PCASP/CAS (Figure 1d), and less than 0.15 ppm of CO (Figure 1c). The sections below use the regional statistical data from Table 4 in conjunction with the lat/lon plots in Figures 2 and 3 to characterize in detail each plume region, with emphasis on the *differences* from one region to the next. This allows us to both quantify large-scale patterns as well as to visualize small-scale changes, and to account for any differences in sample size. Note that discussion of large aerosols has been omitted, as their fractions are negligible, although Figure 3 and Table 4 contain the available information on these particles. Also note that discussion of differences in $r_{e(BC)}$ are mostly omitted, as all are likely within the uncertainty of the SP2; however, we retain the regional mean values in Table 4.

Region I

The near-source region contains, on average, the freshest ($-\log[NO_x/NO_y] \sim 0.2$) and darkest (SSA ~ 0.7) particles, as well as the highest mean BC mass and $r_{e(BC)}$ (over 16,000 #/cm³ and 0.070 μm , respectively) (Figure 2). Overall, the region is dominated by small and medium aerosols, with mean fractions of $\sim 57\%$ and $\sim 31\%$, respectively (Table 4). Apart from the BC particles we know to be present from SP2 measurements, very small aerosols are almost absent throughout most of the region, except for two extreme outlier pixels that contain fractions higher than 60% and therefore inflate the mean to $\sim 13\%$ (the median is $\sim 3.8\%$, a value that is more likely representative).

Region II

Compared to upwind, the near-downwind region contains considerably more oxidized, brighter particles, with mean $-\log[NO_x/NO_y]$ and SSA of ~ 0.53 and ~ 0.77 , respectively (Table 4 and Figure 2; as has been mentioned, filter-based SSA measurements tend to bias low under heavy aerosol burdens, so the actual SSA values may be somewhat higher). The mean absolute BC mass concentration decreases nearly two-fold to $\sim 8,600$ #/cm³, although it is higher within the central portion of this region compared to the plume edges (Figure 2c), where there is entrainment of fresh air. The mean CO-normalized BC mass concentration also decreases significantly, although the median increases. In the central, along-plume transect, there are dramatic increases in both the CO-normalized absorption attributed to BrC (over 25% on average) and the CO-normalized ultraviolet (UV) scattering (38% on average) (Table 4). The CO-normalized CCN₁₅ and aerosol concentrations both increase by more than 80% from Region I. Aerosol size decreases compared to upwind, with increasing fractions of small and very small particles along with a decreasing fraction of medium aerosols. However, this change is only seen along the plume boundaries (Figure 3), where the fraction of very small particles is $\sim 20\text{-}50\%$ higher than the rest of the region, and similarly, medium aerosol fractions are 20-50% lower. Overall, the central, major portion of the plume appears to show no great differences in the partitioning of aerosol size categories compared to upwind, but SSA, aerosol oxidation, BrC absorption, UV scattering, and normalized CCN₁₅ concentration increase measurably, and BC mass concentration decreases.

Region III

The mid-downwind region displays further oxidation and SSA enhancement (means of ~ 0.79 and ~ 0.78 , respectively). Unsurprisingly, this is accompanied by a plume minimum in mean BC mass concentration. Mean CO-normalized BC mass concentration decreases again from Region II, while median concentration slightly increases. CO-normalized UV scattering slightly increases compared to Region II, whereas the mean and median CO-normalized BrC absorption slightly decrease and slightly increase, respectively (and the mean still remains much higher than that of Region I). Furthermore, both the normalized CCN₁₅ and normalized total aerosol count peak in this region (Figure 2). There is also a $\sim 10\%$ regional-mean increase in the fraction of very small aerosols, accompanied by a corresponding decrease in medium and small aerosol fractions (Table 4, Figure 2). These patterns are clearly driven by the southern flank of the region (Figure 3), where there is *particular* enhancement in the very small aerosol fraction, SSA, oxidation, and normalized aerosol and CCN₁₅ concentration compared to the northern flank. Particles in the southern flank are overwhelmingly very small and highly oxidized, and some reach SSA greater than 0.9. Note that the BBOP aircraft did not sample Region IV in the plume, as observed by MISR and MODIS (Figure 1).

II. Satellite Observations of the Government Flats Complex Fire

Table 5 quantifies the mean, standard deviation (SD or σ), and median values for the satellite observations for each region. The four subsequent sections provide qualitative analysis and context for these statistics, with an emphasis on *differences* between regions. It is important to reiterate that when discussing specific particle types (e.g., black carbon, brown carbon, dust, non-absorbing aerosols), the retrieved aerosol properties represent the optical equivalent of the aerosol present; i.e., the true aerosol can be a blend of the size, shape, spectral slope, and absorption of the retrieved components, and is not necessarily a mixture of the specific, retrieved components themselves.

Region I

The near-source region is strongly characterized by high REPA, with a mean SSA of 0.86 and a low SD indicating little variability (Figure 4). This can be attributed to: 1) a very large fraction of spectrally flat, BC-like components throughout the region, with a mean contribution of 56% to the total mid-visible AOD (and upwards of 90% in some pixels); 2) an almost zero AOD fraction of non-absorbing aerosols (mean $\sim 10\%$, median nearly 0%); and 3) a significant AOD fraction of non-spherical aerosols (mean $\sim 20\%$), which are weakly absorbing and represent “dust” analog (possibly soil) particles. There are also some pixels with noteworthy fractions of spectrally steep BrC-like aerosols, but their contribution in Region I (mean $\sim 13\%$, median $< 1\%$) pales in comparison to BC. Regional REPS is overall small, with a mean extinction Ångström exponent (ANG) of 1.54. However, REPS is more variable than SSA due to several lower-ANG pixels along the region’s southwest edge, so the mean may overestimate true particle size (median ANG=1.58; Figures 4-5, Table 5). Component analysis indicates the REPS is the result of a mixture of very small and large aerosols, the latter likely primarily nonspherical particles (Figure S3).

Region II

The near-downwind region displays significantly lower REPA (mean SSA ~ 0.93), marked by a decrease in BC, BrC, and dust-analog fractions and an increase in non-absorbing component fractions (means $\sim 36\%$, 8% , 11% , and 44% , respectively). REPS is also higher here than in Region I, although overall still considered small (mean ANG ~ 1.32). Geographic variability within the region can explain the large SDs in Table 5 – the central area is darker and dominated by BC and some dust-like particles similar to Region I, whereas the areas adjacent to the plume boundaries contain mostly non-absorbing particles, with essentially no non-spherical particles (Figures 4-5, Table 5). Furthermore, the southern portion of the region is retrieved as a mixture of large and very small aerosols, whereas the northern portion is dominated by medium and small aerosols (Figure S3).

Region III

The mid-downwind region displays REPA similar to Region II, although slightly darker overall, with a mean SSA of 0.92. However, there is significant geographic variability in the particle brightness between the northern vs. southern halves when the region is split lengthwise along the plume central axis. The SSA is much higher in the northeast than in the southwest. The entire region is distinct in that it is the only one to contain widespread, significant fractions of BrC-like components, based on the retrievals (regional mean ~30%, a 30-fold increase from upwind). This is accompanied by a corresponding overall regional decrease in the mean/median AOD fractions of the BC, dust, and non-absorbing particle analogs. However, the southern half of the region contains a BC fraction that appears at least equal to BrC. Furthermore, non-absorbing particles make a negligible contribution here, and there is a detectable fraction of the dust analog (~20-30%), all contributing to the low SSA overall. The northeast part of the region is dominated by both BrC and non-absorbing particles, whereas BC and dust fractions are nearly zero, which raises the SSA here. Despite the geographic variability in absorption, ANG is consistent throughout the region, with a mean of 1.82, the highest of all four regions (Figures 4-5, Table 5), indicating a predominance of smaller particles. Component analysis indicates both absolute and fractional increases in small aerosols (Figure S3).

Region IV

The far downwind region contains both the brightest and largest particles in the plume, with a mean SSA of ~0.97 and a mean ANG of ~1.04, so the region is still fine-mode dominated. The coverage in this region is not as extensive as in the other three, but one can still see somewhat coarse particles of $ANG < 0.7$ along the plume edge, and somewhat finer-mode particles further upwind. Based on the retrievals, the region is largely dominated by non-spherical and non-absorbing components, the former being particularly evident at the plume edge. Both BC and BrC component fractions approach null (Figures 4-5, Table 5).

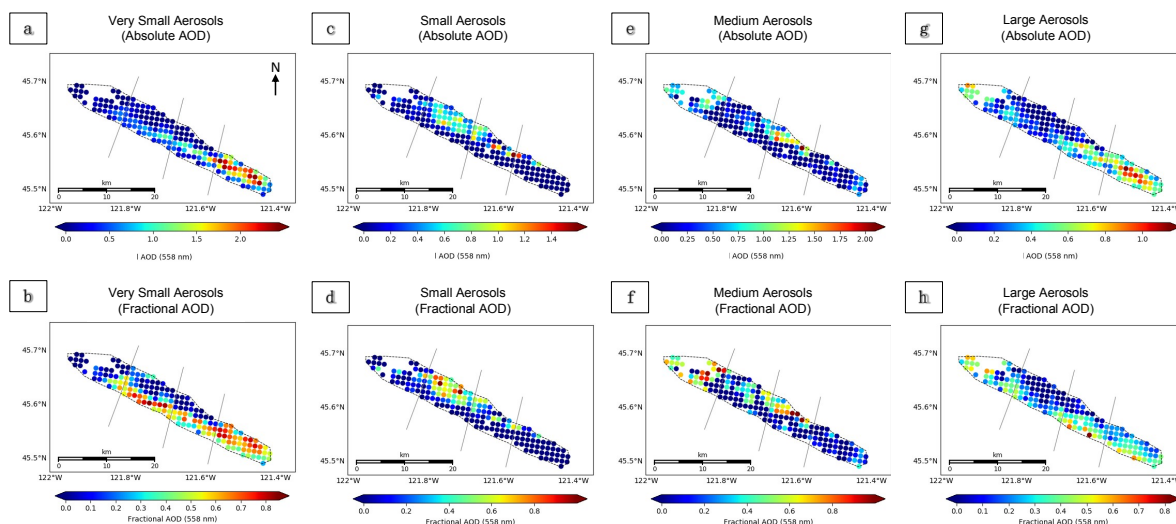


Figure S3. Absolute (top row) and fractional (bottom row) AOD of the four main particle size bins retrieved by the MISR RA for the Government Flats Complex Fire. Note: scales differ between categories.

Supplementary Material, Part 3

We present in the third part of this supplement detailed descriptions of the *in situ* and spacecraft observations collected for the Colockum Tarps Fire and the Douglas Complex Fire (briefly summarized in Section 3.4.1 and 3.4.2 of the main text). The aircraft and satellite observations of these fires were each separated by a day, which reduces their usefulness for formal validation of the satellite retrievals, but demonstrates the value in applying the satellite data in the vast number of situations where such data are available, but *in situ* data are lacking.

I. Colockum Tarps Fire

The Colockum Tarps Fire, first ignited due to human causes, burned from July 25th, 2013 through August 15th, 2013 in southern central Washington. The primary fuel was a mixture of grass, brush, and timber; over 80,000 acres burned in total [59]. The July 26th, 2013 BBOP research flight and the subsequent July 27th MISR overpass observed the resulting smoke plume. Plume geometry changes significantly between observations; the plume extends toward the northeast from the fire source on July 26th, and toward the southeast on July 27th. The plume outline for the *in situ* observations was traced using the RGB MODIS Aqua image from ~20:10 UTC (Figure S4a; the aircraft flew in the area from ~20:00-22:20 UTC). There is a significant pocket of little-to-no smoke within the plume boundaries at this time, but as plume dynamics and smoke location may have changed during the course of the flight, we include this area within the boundary.

Measurements are considered “outside” the plume in areas where CO and aerosol concentrations were below thresholds of 0.11 ppm and 1000 #/cc, respectively, where measurements are particularly noisy, or where the plane was flying at an altitude thought to be above the smoke layer. These requirements usually all coincide (Figure S4c, d), and aircraft data obtained for points considered “outside” the plume, under very low particle concentration, are generally quite uncertain (e.g., the very low SSA values outside the plume boundaries in Figure S5a). Note also that the southern along-plume transect was flown at ~12:15 UTC, the very beginning of the ~2.5-h sampling period. As such, the seemingly anomalous along-plume data between cross-plume transects 3 and 4 in Figures S5 a, b, and c was probably outside the plume boundary at acquisition time, unlike the geographically nearby cross-plume transects obtained an hour or more later. The following day, as shown in the broader-swath MODIS imagery (Figure S4b), MISR sees some, but not all, of the visible plume extent.

Aircraft Observations of the Colockum Tarps Fire

The flight observations depict a plume with particle properties that appear to change less systematically with downwind distance than the Government Flats Complex Fire, making it difficult to divide the plume neatly into characteristic regions as was done in Section 3 of the main text. From the measured wind speeds, we estimate the visible plume age to be ~226 minutes (~3.8 h) along the cross-plume transect indicated by the line in Figure S4a at the time of the flight.

Particle properties vary on short spatial scales (~1 km); however, some larger-scale patterns are also evident. There is an area of optically very thick smoke in the apparent source region(s), characterized by high total aerosol count, oxidation state, SSA, CCN concentration, and BC fraction and concentration, relative to background over most of the plume extent (Figures S4 and S5). However, very near the source, the particles are highly light-absorbing, with oxidation values near zero and SSA of 0.75 or lower – these SSA values are expected to be biased low due to measurement bias with the PSAP. In general, the plume is dominated by “small” particles, with “very small” particles contributing second-most, based on particle counts, and moderate contributions from medium aerosols in some areas (Figure S6). Large particles are essentially absent, with fractional contributions well below 1%. When split lengthwise along the plume’s

central axis, the plume displays somewhat larger particle size toward the northern edge, where medium aerosols contribute up to 20% of the total aerosol count. The fraction of small aerosols is also somewhat higher here, whereas very small particles make up a noticeably smaller fraction. From plume source to nominal end, particle size overall appears to increase slightly along the plume central axis, to the extent this is sampled by the aircraft.

As mentioned above, particles sampled along the cross-plume aircraft transect closest to the source are highly absorbing and very fresh (Figures S5a and S5b). Both CCN number and BC mass concentrations also peak near the source, as might be expected. BC and CCN concentrations decrease considerably downwind within the near-source region, and oxidation state increases. There is also an increase in the CO-normalized aerosol concentration between the first two near-source, cross-plume aircraft transects (Figure S5f), indicating possible new particle formation shortly after emission, but there is no evidence in these data for additional particle production further downwind, and the increased concentration could arise from wind-driven convergence or changing emission at the source. Downwind of the first, near-source transect, SSA increases gradually over the length of the plume, BC and CCN concentrations remain relatively constant, whereas oxidation state and normalized CCN concentration are more variable. Toward the plume end (~226 minutes of aging), particles are only moderately absorbing (SSA ~0.9), are oxidized substantially ($-\log[\text{NO}_x/\text{NO}_y] > 0.6$) and contain considerably less BC mass contributing to the overall aerosol mass loading. The gradual increase in SSA downwind, despite relatively constant BC fraction, could be due to particle hydration, as the small-particle fraction increases relative to the very small particle fraction. It could also be due to the condensation of VOC's onto existing aerosols, leading to increasing particle diameter of OA and increased coating thickness of BC-containing particles. Most BC-containing particles are less than 0.1 μm in radius, with smaller sizes of ~0.06 μm closest to the source and larger particles, ranging from 0.07 up to 0.1 μm , downwind. Overall, $r_{e(\text{BC})}$ does not follow any systematic spatial pattern in the available data (Figure S7).

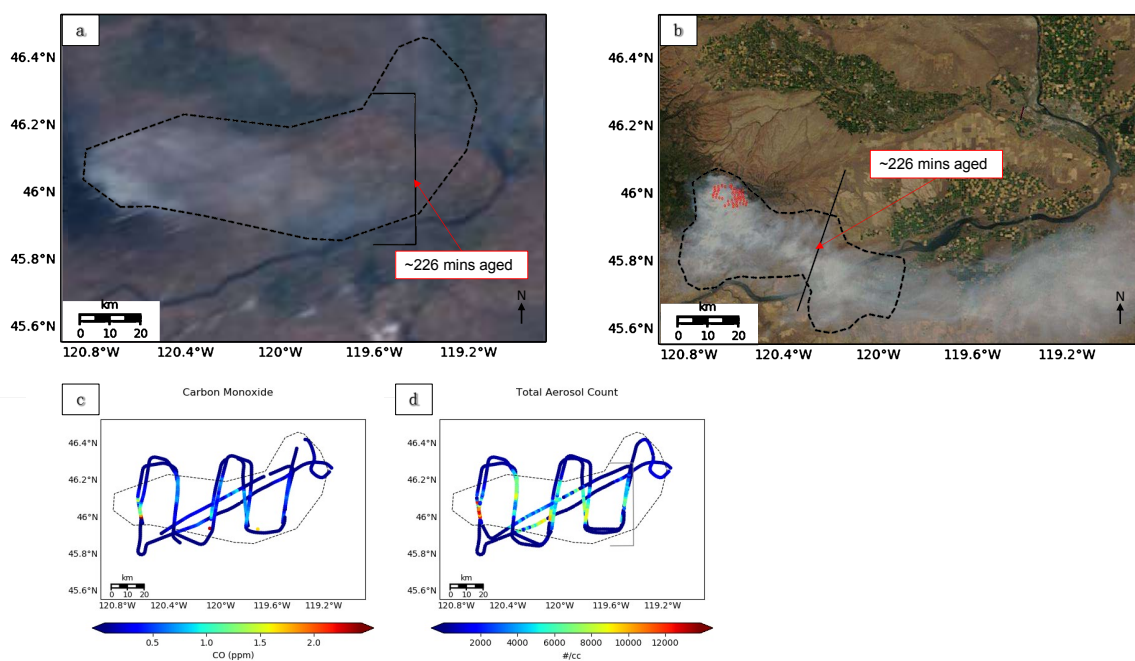


Figure S4. The Colockum Tarps fire in southern central WA as seen: **(a)** during BBOP flight operations, ~20:00-22:20 UTC on July 26th, (20:10 UTC, MODIS Aqua RGB image), and **(b)** at MISR overpass time on July 27th (19:13 UTC, MODIS Terra RGB image). The red dots indicate MODIS-identified hot spots and are used to estimate source location. The near-source plumes are outlined with thin dashed lines in these figures, and the

location of smoke within the plume estimated as having aged ~3.8 hours is marked with a thin solid line. Panels (c) and (d) are maps of the aircraft *in situ* CO and total aerosol count measurements on July 26th, respectively.

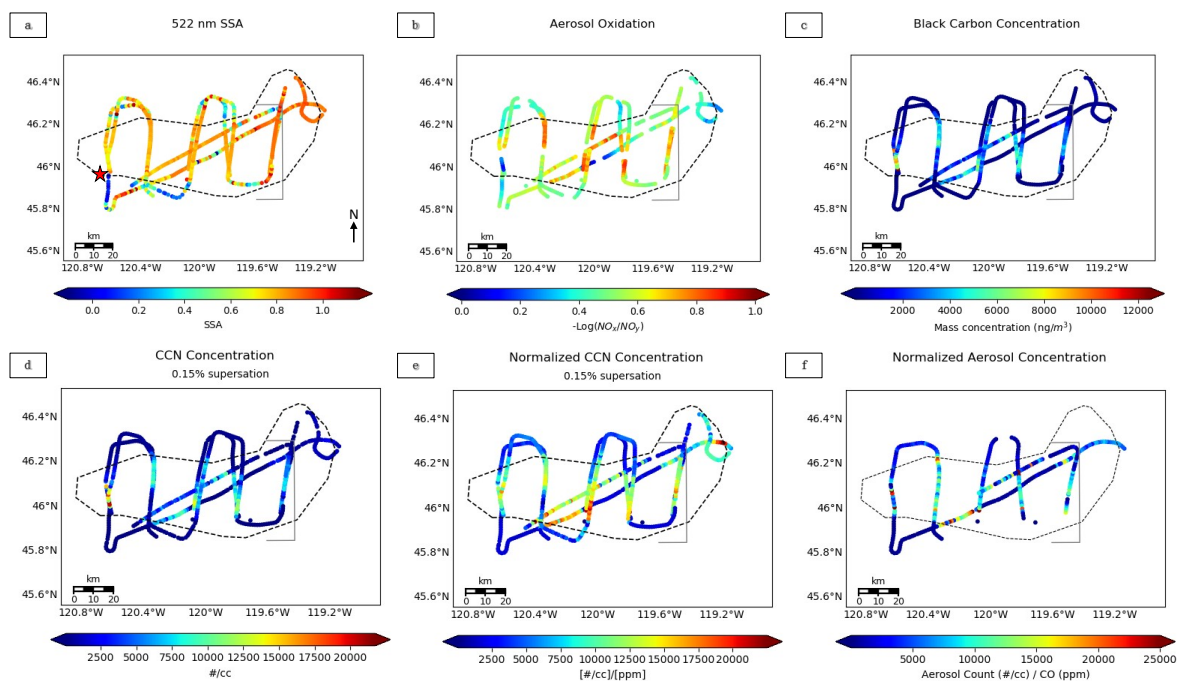


Figure S5. Aircraft observations from the Colockum Tarps fire in southern central WA of (a) 522-nm SSA (PSAP/neph), (b) aerosol oxidation (derived from 3-channel Oxides of Nitrogen Analyzer), (c) Mass concentration of BC and size of BC-containing particles (SP2), (d) the concentration of particles that can act as CCN at 0.15% supersaturation (CCN-200 instrument), (e) the CCN concentration divided by the CO concentration, and (f) the total aerosol concentration divided by the CO concentration. The star in (a) serves a reminder of the source location.

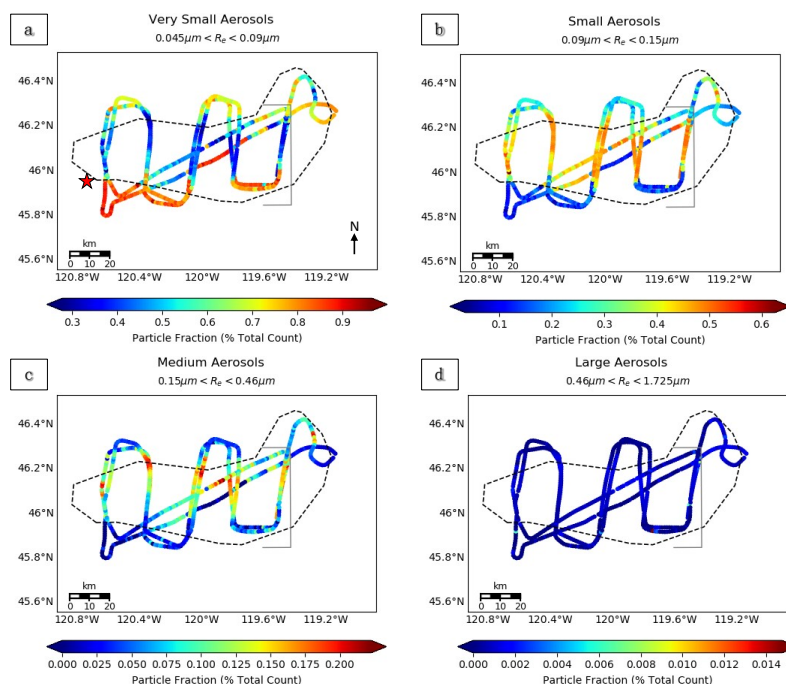


Figure S6. Fractional contributions to the total aerosol count for very small (a), small (b), medium (c), and large (d) aerosols in the Colockum Tarps fire in southern central WA, as measured by the PCASP and CAS *in situ* instruments. The star in (a) serves a reminder of the source location. Note: scales differ between categories.

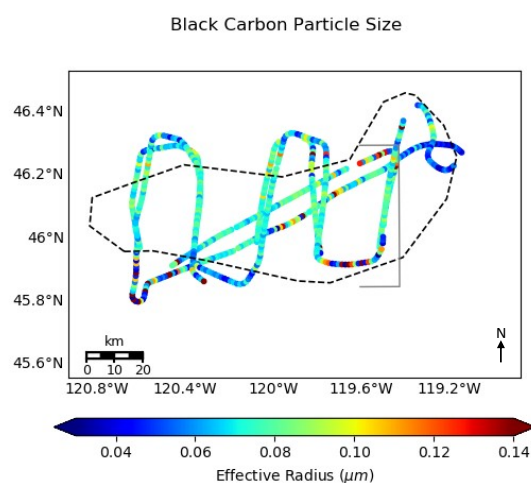


Figure S7. $r_{e(BC)}$ for the Colockum Tarps fire observed by the SP2 aboard the BBOP G-1 aircraft.

MISR Observations and Discussion for the Colockum Tarps Fire

The next-day satellite observations show significant changes in plume geometry. The plume boundaries are better defined on this day (Figure S4), and the satellite retrievals provide significant context beyond the aircraft transect observations. MISR-MINX stereo heights indicate the smoke stays mostly below 4 km and has a median height of ~ 2.9 km ASL (Figure S8a-b). Approximately 40 km downwind, the smoke becomes lofted about 1 km higher than the upwind area. At around this distance, the plume age is ~ 226 minutes (~ 3.8 h), as estimated from wind speed roughly along the plume axis, at plume elevation

(Figure S8c). The smoke is also optically very thick, with a nominal-retrieved mid-visible AOD near the source of 9, though the uncertainty in retrieved AOD becomes large once AOD exceeds a value of 4 or 5. The extinction Ångström exponent (ANG) suggests the plume at this time is dominated by small-to-very-small particles overall (median ANG ~ 1.74), particularly near the source (Figure S8e). Component analysis suggests heavy weighting of very small aerosols near the source, and a mixture of mostly small but also some medium particles downwind, with a near-complete lack of larger particles, as on the previous day (Figure S9).

As expected, the particles are darkest near the source. There is a patch of very small, dark particles extending from the source to about 20 km downwind along the northern boundary of the plume, with SSA ~ 0.83 or lower and ANG ~ 3.0 or higher. However, the particles brighten downwind and to the south, with SSA above 0.97 in some places (median plume SSA ~ 0.90) (Figure S8f). The SSA values and their observed increase with age is consistent with that reported by *Sedlacek et al.* [19]. Further analysis of the RA components suggests that particles near the source are primarily a mixture of BC- and BrC-like aerosols, with some nonabsorbing particles, but that BrC is confined near the source so that the downwind region is retrieved entirely as BC and non-absorbing aerosols (Figure S10), yielding a net mid-visible SSA ~ 0.93 . The apparent, abrupt particle-type transition might indicate changes in the burning conditions at the fire rather than particle evolution after emission.

Taken together, the satellite and *in situ* observations describe a plume with fine-mode, highly absorbing particles near the source that become brighter downwind. The MISR RA differs from the aircraft measurements in that it derives mostly very small particles near the source, with a significant increase in particle size a short distance downwind, whereas the aircraft CAS and PCASP observe particles *in situ* that are mostly in the same small size category throughout the plume (with pockets of enhanced medium particle fractions, similar to the pockets of lower ANG in the MISR RA). The difference in initial particle size could reflect changes in smoke properties between the two days or could be due to *in situ* measurement selective sampling, whereby plume properties would be more completely represented when the entire region is mapped with satellite observations.

The upper ranges of observed SSA values between the two days are very similar; in both cases, highly scattering aerosols, having SSA above 0.95, appear far from the source. As mentioned in the discussion of the Government Flats Complex Fire, the fact that the RA does not observe SSA as low as the aircraft could be due to the finer spatial resolution at which the aircraft samples, the limitations of filter-based measurements, or to limitations in the RA particle climatology. Regardless, the same general light-absorption patterns apparently persist day to day for the Colockum Tarps Fire. A more noticeable difference is that BC mass concentration peaks near the source and decreases threefold after the first cross-plume transect, and then appears relatively constant further downwind during aircraft operations on July 26th (Figure S5c), whereas on July 27th, the MISR RA indicates that BC AOD varies but preserves high values in patches over much of the plume downwind (Figure S10a-b). This difference could also be explained by limited aircraft sampling, though changing fire emissions cannot be ruled out.

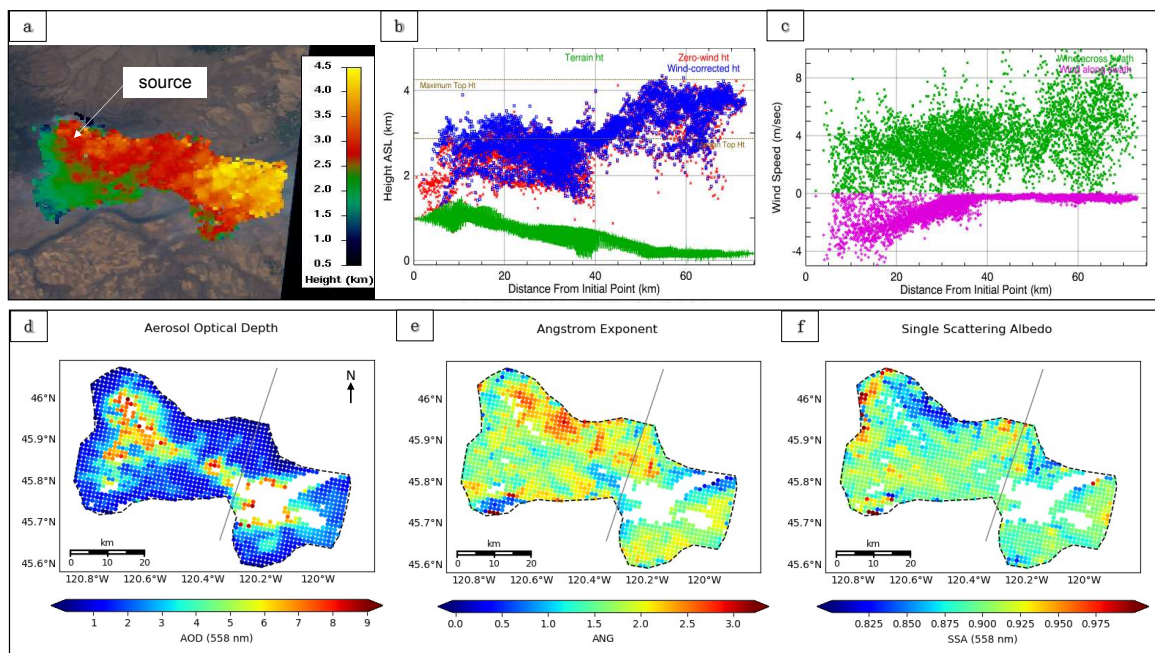


Figure S8. Plume properties for the Colockum Tarps fire in southern central WA retrieved by MISR at 19:13 UTC (Orbit 72382, Path 46, Blocks 53-54). **(a)** MISR-MINX stereo height retrieval map, **(b)** MINX stereo height profile as a function of distance from the source, for both zero-wind (red) and wind-corrected (blue) analyses, with surface elevation indicated in green, **(c)** the MINX-derived across-swath and along-swath wind vectors at plume level, **(d)** the RA-derived AOD at 558 nm, **(e)** ANG, and **(f)** the SSA at 558 nm. The transect for plume age estimated at ~226 minutes is indicated with a thin gray line in panels d-f.

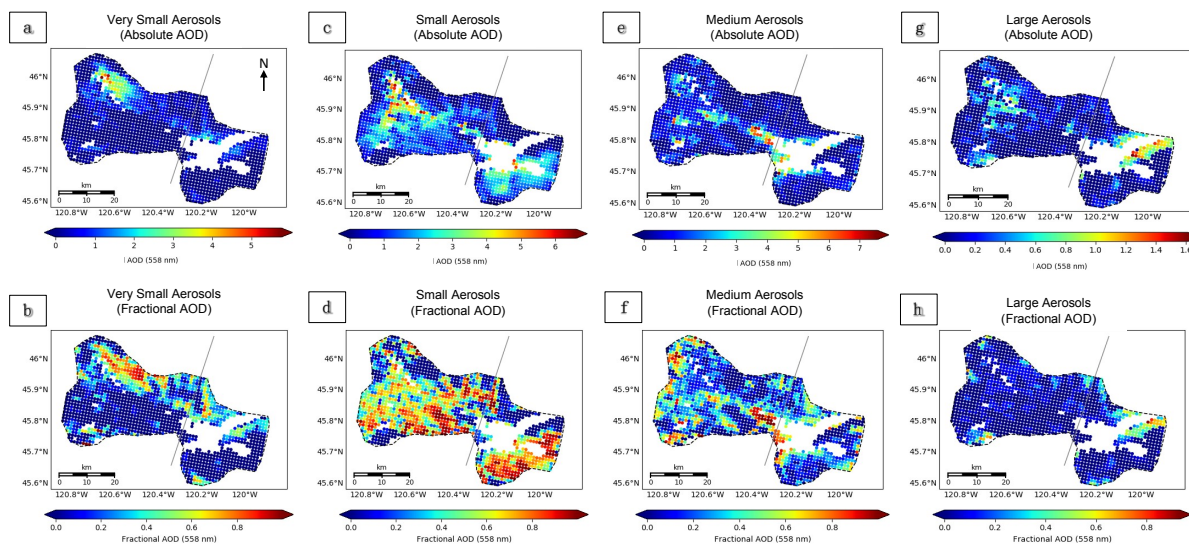


Figure S9. Absolute (top row) and fractional (bottom row) AOD of the four main particle size bins retrieved by the MISR RA for the Colockum Tarps fire. Note: scales differ between categories.

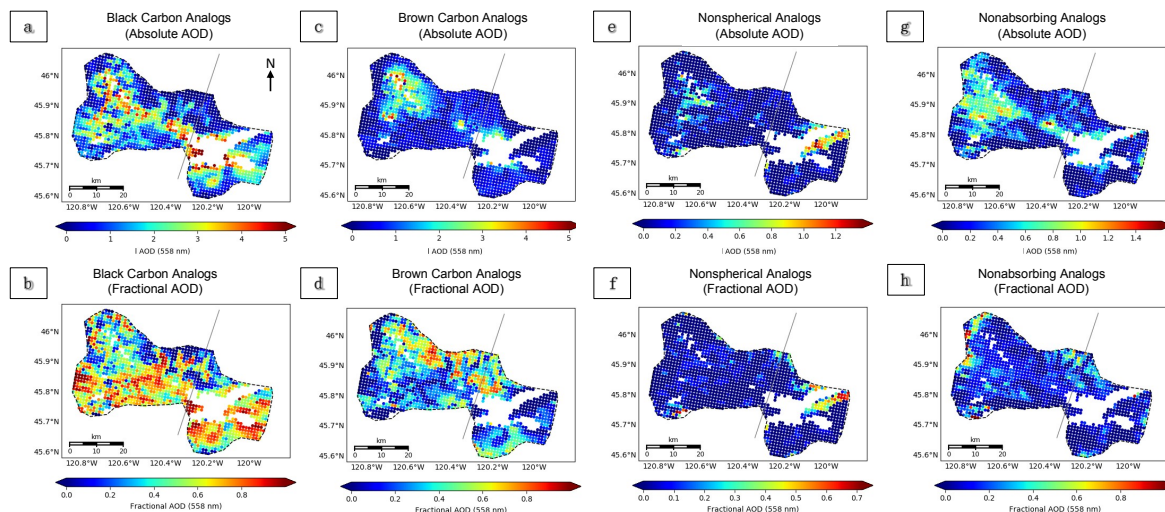


Figure S10. The absolute and fractional AOD of various MISR components, for the Colockum Tarps fire in southern central WA, where (a-b) are the sum of all “flat,” i.e., BC-like components, (c-d) are the sum of all “flat,” i.e. BrC-like components, (e-f) are the non-spherical dust-like component, and (g-h) are the sum of all non-absorbing components.

II. Douglas Complex Fire: Satellite Observations Preceding Aircraft Observations

The Douglas Complex fire was a large system originally comprised of dozens of lightning-sparked fires that ignited on July 26th, 2013 and burned through August 19th, 2013 in southern coastal Oregon. The fuel was a mixture of old growth and second growth conifer [58]. The August 5th, 2013 MISR overpass and the subsequent August 6th BBOP research flight observed the smoke plumes that were produced (Figure S11). The outline for the *in situ* observations was traced from the MODIS-Terra RGB image at 19:51 UTC (flight operations took place in the area from approximately 19:30-21:00 UTC). As one can see in Figure S11b, the plume outline selected does not fully capture all of the smoke in the scene; it is just meant to provide a reference for the apparent core region of the plume.

MISR Observations of the Douglas Complex Fire

On August 5th the plume had a well-defined plume core (Figure S11a), with AOD exceeding the nominal MISR RA AOD upper limit of 9 (Figure S12d), with a large uncertainty. The plume does not rise above 2.0 km ASL, and median smoke height is ~1.17 km ASL, which is not much above the terrain in this topographically complex region (Figure S12b). Wind speeds are low throughout the observed area (Figure S12c), which might explain the difficulty in locating the plume source, as the smoke tended to pile up over a small area. MISR-retrieved particle size and light-absorption data indicate the plume core is dominated by small-medium, moderately absorbing aerosols ($ANG \leq 1$, $SSA \sim 0.87-0.92$), whereas the surrounding, lower-AOD areas contain smaller, weakly or nonabsorbing particles ($ANG > 1$, $SSA \sim 0.92-1.0$) (Fig. S12e, S12f). Component analysis reflects the larger REPS and lower REPA in the plume core than the surroundings (Figures S12 and S13). Spectrally steep BrC and non-spherical dust optical analogs are also retrieved, concentrated in the core (Figure S14c-d and e-f, respectively). The retrieved non-spherical component suggests there may be externally mixed dust or soil particles ejected into the atmosphere during intense burning, or a lack of spherical particles of similar size distribution and SSA to the dust analog in the algorithm climatology (Table 2).

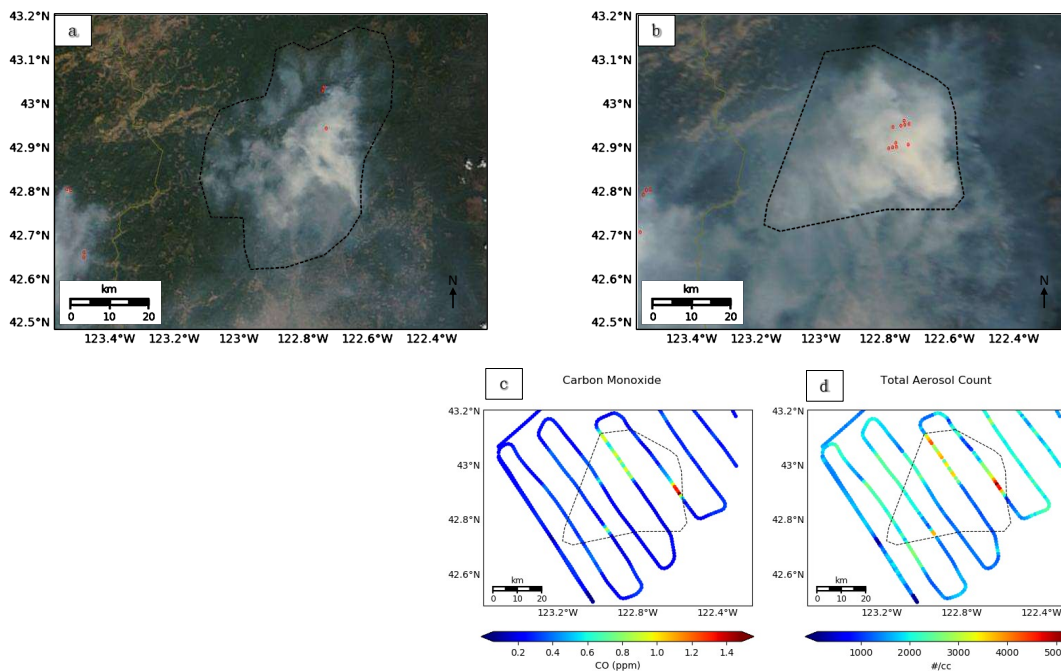


Figure S11. The Douglas Complex fire in southern coastal OR as seen: **(a)** at MISR overpass time on August 5th (19:08 UTC; MODIS Terra RGB image), and **(b)** during BBOP flight operations ~19:30-21:00 UTC on August 6th (19:51 UTC; MODIS Terra RGB image). The red dots indicate MODIS-identified hot spots, and are used to estimate source location. Panels **(c)** and **(d)** are maps of the aircraft CO and Total Aerosol Amount on August 5th, respectively.

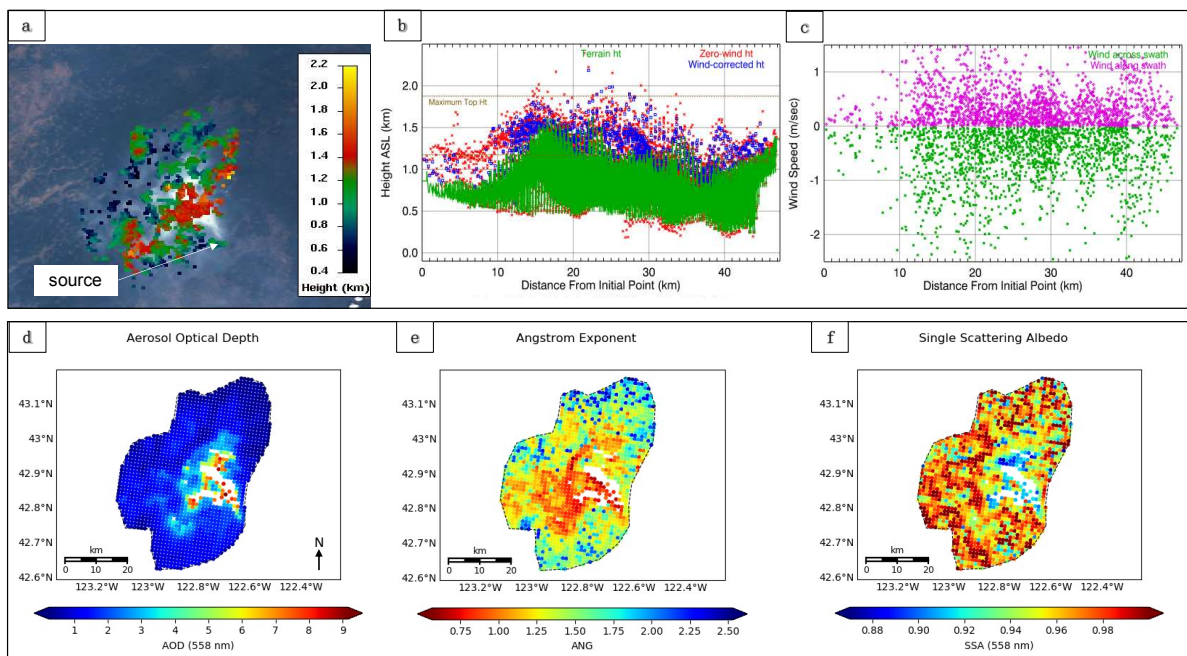


Figure S12. Plume properties for the Douglas Complex fire in southern coastal OR retrieved by MISR at 19:08 UTC (Orbit 72513, Path 45, Block 56). **(a)** MISR-MINX stereo height retrieval map, **(b)** MINX stereo height profile as a function of distance from the source, for both zero-wind (red) and wind-corrected (blue) analyses,

(c) the across-swath and along-swath wind vectors, (d) the RA-derived AOD at 558 nm, (e) ANG, and (f) the SSA at 558 nm.

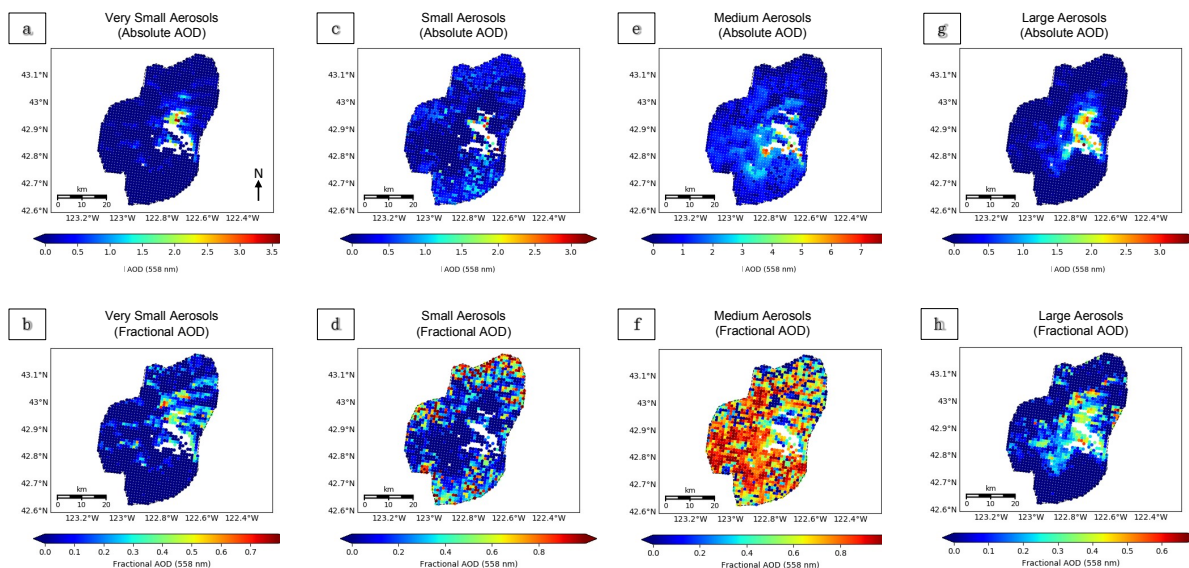


Figure S13. Absolute (top row) and fractional (bottom row) AOD of the four main particle size bins retrieved by MISR for the Douglas Complex fire. Note: scales differ between categories.

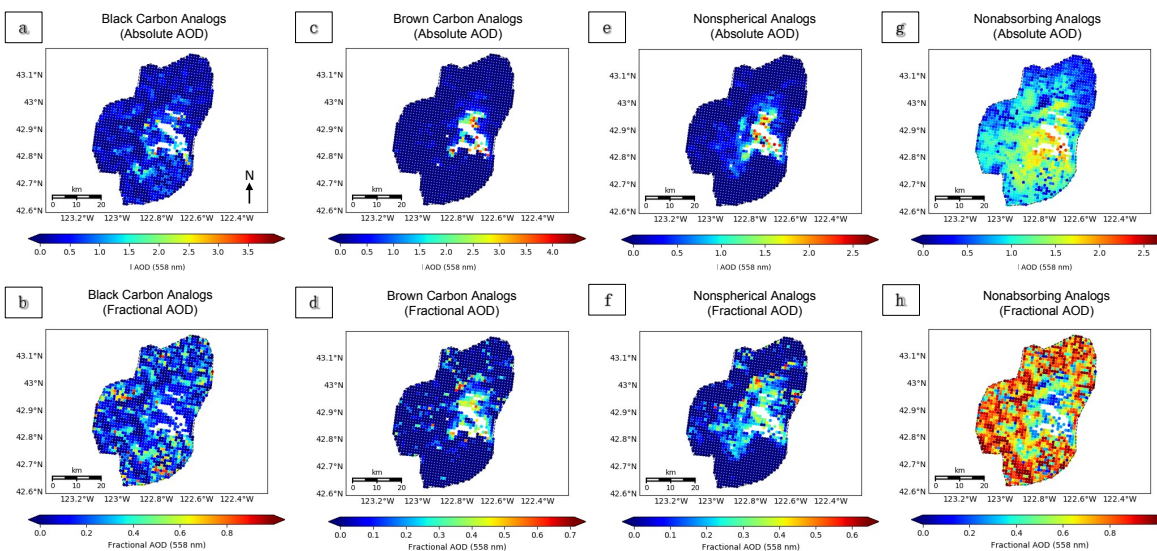


Figure S14. The absolute and fractional AOD of various MISR components for the Douglas Complex fire in southern coastal OR, where (a-b) are the sum of all “flat,” i.e. BC-like components, (c-d) are the sum of all “flat,” i.e. BrC-like components, (e-f) are the non-spherical dust-like component, and (g-h) are the sum of all non-absorbing components.

Aircraft Observations and Discussion for the Douglas Complex Fire

The BBOP *in situ* plume observations on the following day describe a scene with an expanded plume core area and considerable, diffuse smoke in the immediate surroundings (Figure S11b). The maximum CO and aerosol concentrations in the available measurements are located near the MODIS-identified hot spots (Figure S11c-d), but the aircraft did not fly directly over these spots, so the actual distribution is ambiguous. The sampled near-source areas also contained some of the brightest and the most highly oxidized particles in the available data record (Fig. S15a, b). However, they also contain the most BC mass of this plume (Figure S15c), though much less than the sampled regions of the Government Flats and July 26th Colockum Tarps fire plumes. (This could be a consequence of the elevation at which the aircraft sampled rather than the peak smoke concentrations of the Douglas Complex fire.) The particles in the plume core are primarily small and medium in size, whereas the particles in the surroundings are mostly very small and small (Figure S16). BC effective particle size ($r_{e(BC)}$) shows no distinct pattern over the aircraft-sampled region (Fig. S17).

The combined information from the satellite and the aircraft data suggest larger particle sizes in the thickest parts of the plume compared to the surroundings. These particles fall within the small to medium size range; however, the RA retrieves overall slightly larger particles than the aircraft data on the previous day, including a significant contribution from large particles in the plume core. Particles near the source are moderately light-absorbing as seen by MISR (SSA ~ 0.92) but are brighter the next day during flight operations (SSA ~ 0.95), when the fire appears to be a bit more active in the imagery (Figure S11).

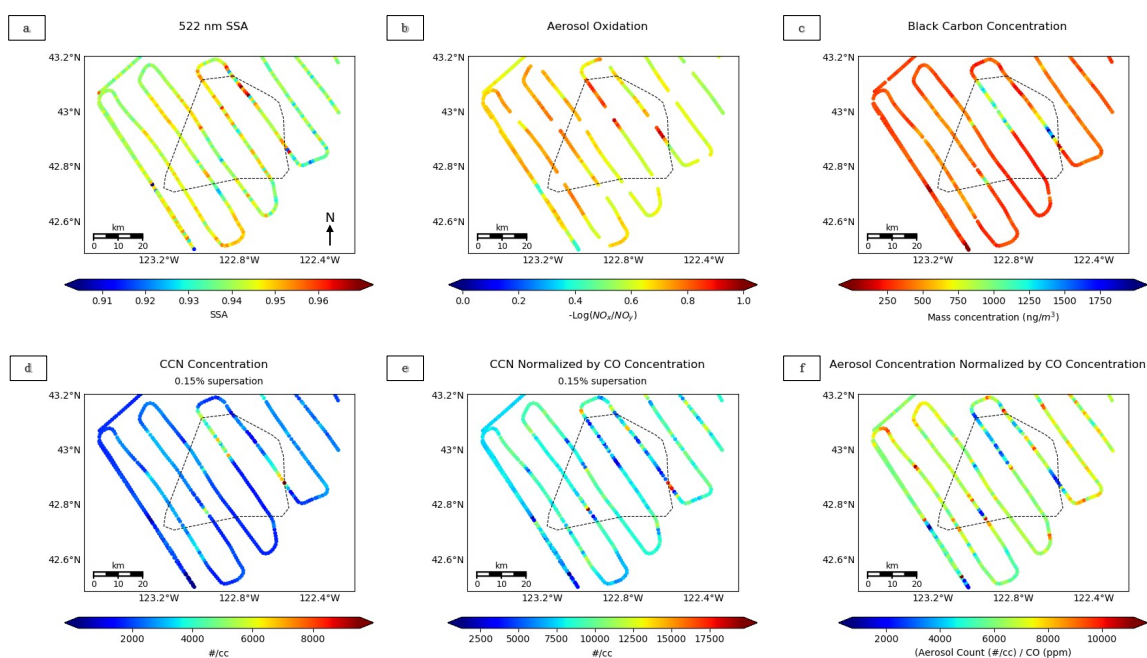


Figure S15. Aircraft observations from the Douglas Complex fire in southern coastal OR of (a) 522-nm SSA (PSAP/neph), (b) aerosol oxidation (derived from 3-channel Oxides of Nitrogen Analyzer), (c) Mass concentration of BC and size of BC-containing particles (SP2), (d) the concentration of particles that can act as CCN at 0.15% supersaturation (CCN-200 instrument), (e) the CCN concentration divided by the CO concentration, and (f) the total aerosol concentration divided by the CO concentration.

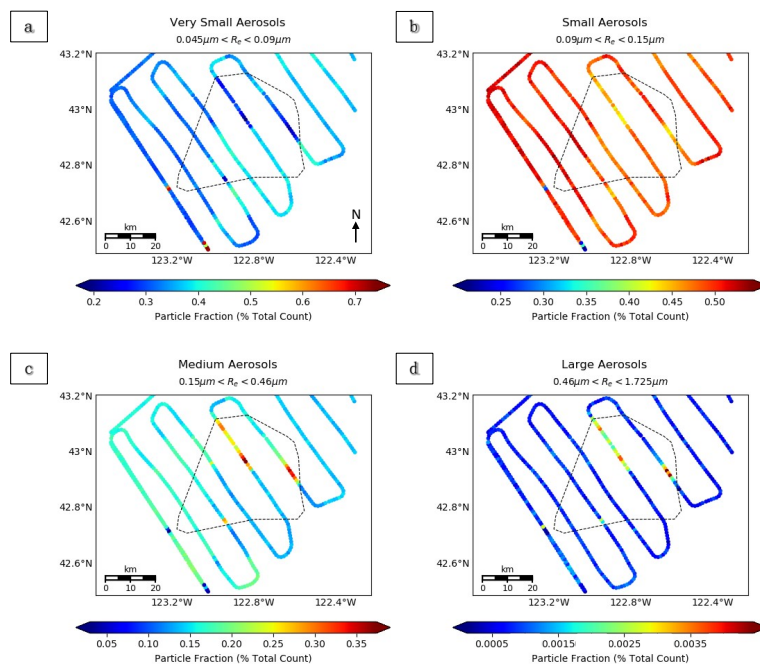


Figure S16. Fractional contributions (from zero to one) to the total aerosol count for very small (a), small (b), medium (c), and large (d) aerosols in the Douglas Complex fire in southern coastal OR, as measured by the PCASP and CAS *in situ* instruments. Note: scales differ between categories.

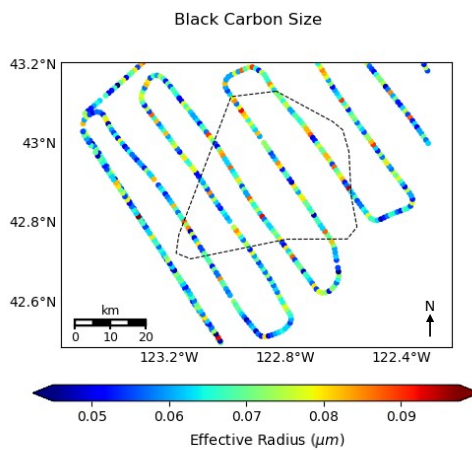


Figure S17. $r_{e(\text{BC})}$ for the Douglas Complex fire, observed by the SP2 aboard the BBOP G-1 aircraft.